Inorg. Chem. **2008**, *47*, 7009−7024

Series of Mixed Valent Fe(II)Fe(I) Complexes That Model the H_{ox} State of [FeFe]Hydrogenase: Redox Properties, Density-Functional Theory Investigation, and Reactivities with Extrinsic CO

Christine M. Thomas,† Tianbiao Liu,† Michael B. Hall,* and Marcetta Y. Darensbourg*

Department of Chemistry, Texas A&M University, College Station, Texas 77845

Received April 11, 2008

A series of asymmetrically disubstituted models of the active site of [FeFe]-hydrogenase, (μ-pdt)[Fe(CO)$_2$PMe$_3$][Fe(CO)$_2$NHC] (pdt = 1,3-propanedithiolate, NHC = IMes, 1,3-bis(2,4,6-trimethylphenyl)imidazol-2-ylidene IMes (**1**), IMesMe, 1-methyl,3-(2,4,6-trimethylphenyl)imidazol-2-ylidene (**2**) or IMe, 1,3-bis(methyl)imidazol-2-ylidene (**3**)), have been synthesized and characterized. The one-electron oxidation of these complexes to generate mixed valent models of the H_{ox} state of [FeFe]-hydrogenase, such as the previously reported (μ-pdt)(μ-CO)[Fe(CO)$_2$PMe$_3$][Fe(CO)IMes]$^+$ (**1$_{ox}$**) (Liu, T.; Darensbourg, M. Y. *J. Am. Chem. Soc.* **2007**, *129*, 7008−7009) has been examined to explore the steric and electronic effects of different N-atom substituents on the stability and structure of the mixed valent cations. The differences in spectroscopic properties, structures, and relative stabilities of **1$_{ox}$**, (μ-pdt)[Fe(CO)$_2$PMe$_3$][Fe(CO)$_2$IMesMe]$^+$ (**2$_{ox}$**), and (μ-pdt)[Fe(CO)$_2$PMe$_3$]-[Fe(CO)$_2$IMe]$^+$ (**3$_{ox}$**) are discussed in the context of both experimental and theoretical data. Of the three derivatives, only that with greatest steric bulk on the NHC ligand, **1$_{ox}$**, shows a clear indication of a μ-CO by solution ν(CO) IR and yields to crystallization as a rotated form, commensurate with the two-Fe subsite of H_{ox}. In addition, the reactivity of the complexes with extrinsic CO to form CO adducts and/or exchange with ^{13}CO is explored by experiment and by using density-functional theory calculations.

Introduction

The unique dihydrogen chemistry of hydrogenases, that is, catalysis of H_2 production and reversible H_2 uptake at remarkable efficiency, has inspired biochemists and chemists in two aspects concerned with the global energy issue: (1) cheap electrocatalysts for H_2 evolution; (2) new, more economical electrode materials as alternatives to platinum in fuel cells.[1]The structural resemblance of the diiron subunit in the H-cluster of the active site of [FeFe]H_2ase[2] to the well-known organometallic complexes, [(μ-RS)$_2$Fe$_2$(CO)$_6$],[3] has enabled synthetic chemists to skillfully construct numerous synthetic analogues with promise for hydrogenase-like function in the absence of the protein superstructure.[4] Most of the Fe^IFe^I complexes thus derived serve as solution electrocatalysts for H_2 production in the presence of acids of varying strengths.[5] Oxidized $Fe^{II}Fe^{II}$ analogues, under CO-loss conditions, have demonstrated the ability to catalyze H/D scrambling in H_2O/D_2 mixtures (or vice versa), indicating their potential function as H_2 oxidation catalysts.[6] Such synthetic homovalent, diamagnetic diiron complexes are much more readily accessed than are the mixed valent, paramagnetic forms readily observed in the H-cluster.

* To whom correspondence should be addressed. E-mail: hall@mail.chem.tamu.edu (M.B.H.), marcetta@mail.chem.tamu.edu (M.Y.D.).
† These coworkers contributed equally.

(1) (a) Adams, M. W. W.; Stiefel, E. I. *Science* **1998**, *282*, 1842–1843. (b) Cammack, R.; Frey, M.; Robson, R. *Hydrogen as a Fuel: Learning from Nature*; Taylor and Francis: London, 2001.
(2) (a) Nicolet, Y.; Piras, C.; LeGrand, P.; Hatchikian, C. E.; Fontecilla-Camps, J. C. *Structure* **1999**, *7*, 13–23. (b) Peters, J. W.; Lanzilotta, W. N.; Lemon, B. J.; Seefeldt, L. C. *Science* **1998**, *282*, 1853–1858.
(3) (a) Darensbourg, M. Y.; Lyon, E. J.; Zhao, X.; Georgakaki, I. P. *Proc. Natl. Acad. Sci. U.S.A.* **2003**, *100*, 3683–3688. (b) Adams, M. W. W.; Stiefel, E. I. *Curr. Opin. Chem. Biol.* **2000**, *4*, 214–220. (c) Evans, D. J.; Pickett, C. J. *Chem. Soc. Rev.* **2003**, *32*, 268–275.
(4) (a) Lawrence, J. D.; Li, H.; Rauchfuss, T. B.; Benard, M.; Rohmer, M.-M. *Angew. Chem., Int. Ed.* **2001**, *40*, 1768–1771. (b) Razavet, M.; Davies, S. C.; Hughes, D. L.; Pickett, C. J. *Chem. Commun.* **2001**, 847–848. (c) Tard, C.; Liu, X.; Ibrahim, S. K.; Bruschi, M.; De Gioia, L.; Davies, S. C.; Yang, X.; W. L.-S.; Sawers, G.; Pickett, C. J. *Nature* **2005**, *433*, 610–613. (d) Justice, A. K.; Zampella, G.; De Gioia, L.; Rauchfuss, T. B.; van der Vlugt, J. I.; Wilson, S. R. *Inorg. Chem.* **2007**, *46*, 1655–1664. (e) van der Vlugt, J. I.; Rauchfuss, T. B.; Whaley, C. M.; Wilson, S. R. *J. Am. Chem. Soc.* **2005**, *127*, 16012–16013.

10.1021/ic800654a CCC: $40.75
Published on Web 07/03/2008

Scheme 1

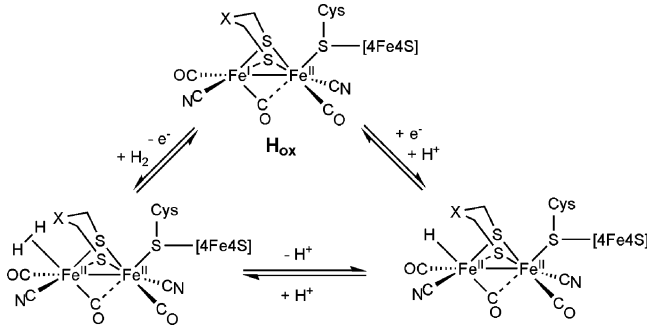

Scheme 2

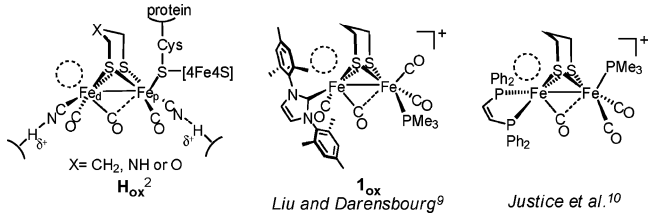

The accepted mechanism for reversible H_2 processing by [FeFe]H_2ase, invokes a stable (crystallographically and spectroscopically characterized)[7] $Fe^{II}Fe^{I}$ species within the redox level designated as H_{ox}.[8] This mixed valent $S = {}^1/_2$ species serves as a starting point for the catalytic activation of H_2 toward heterolytic cleavage from its oxidized $Fe^{II}Fe^{II}$ form, as expressed in the minimal mechanism of Scheme 1. Its reduced $Fe^{I}Fe^{I}$ or $Fe^{0}Fe^{II}$ form leads to oxidative addition of a proton and formation of H_2.

Key to the proton reduction or hydrogen oxidation catalysis mediated by the active site of [FeFe]H_2ase is the open site on the iron, within the two-iron subsite, that is distal to the 4Fe4S cluster, Fe_d (Scheme 2). This open site gives the appearance of a square pyramidal Fe_d which is inverted, or rotated, with respect to a similar square pyramidal geometry about Fe_p. In the former, the bridging or semibridging CO serves as apical ligand while two S donors, a CO, and a CN^- comprise the base. In Fe_p, the apical donor is the cysteinyl sulfur which serves as the sole covalent connection to the protein, and bridges to a redox active 4Fe4S cluster.

With a careful choice of first coordination sphere consisting of abiological ligands, we and others have shown the possibility of isolating stable mixed valent small molecule analogues of this rotated two-iron subsite of the H_{ox} structure.[9,10] These complexes contain an open site on the rotated iron center and a CO that resides underneath the Fe−Fe vector, with varying degrees of bridging versus terminal character according to the substituent ligands. Scheme 2 displays two structural analogues; $\mathbf{1_{ox}}$ is based on a combination of an N-heterocyclic carbene and PMe_3 as substituent ligands. A second example of a rotated $Fe^{II}Fe^{I}$ species from the Rauchfuss group, (μ-SCH_2CH_2S)[$Fe(CO)_2$(PMe_3)][Fe(CO)(dppv)]$^+$ (dppv = 1,2-(diphenylphosphino)-vinylidene), shows greater linearity in the CO that is underneath the Fe−Fe vector with otherwise similar spectroscopic signatures as $\mathbf{1_{ox}}$.[10]

Such breakthroughs in the synthesis of mixed valent $Fe^{II}Fe^{I}$ compounds were presaged by computational studies[11] and by the efforts of Rauchfuss and co-workers, who reported $Fe^{II}Fe^{II}$ dithiolates in which a terminal hydride, {(μ-SCH_2CH_2S)(μ-CO)[$HFe(PMe_3)_2$][$Fe(CO)(PMe_3)_2$]}$^+$ PF_6^-, was characterized, mimicking the structural features of an expected key intermediate of the enzymatic catalysis and highlighting the likely occurrence of a terminal hydride in the catalytic cycle.[4e] Via in situ ^{1}H NMR spectroscopy at low temperatures, Ezzaher, Schollhammer, and co-workers detected a similar terminal hydride species directly generated through protonation of $Fe^{I}Fe^{I}$ dithiolates.[12] Earlier, Pickett, Best, and co-workers reported an $Fe^{II}Fe^{I}$ species, which models the CO-inhibited state of the [FeFe]H_2ase active site, H_{ox}^{CO}, characterized in situ by Electron Paramagnetic Resonance (EPR) and Fourier Transform Infrared (FTIR) spectroscopies.[13]

The $Fe^{I}Fe^{I}$ precursor of the mixed valent $Fe^{II}Fe^{I}$ dithiolate, (μ-pdt)[$Fe(CO)_2PMe_3$][$Fe(CO)_2$IMes] (**1**, pdt = 1,3-propanedithiolate, IMes = 1,3-bis(2,4,6-trimethylphenyl)imidazol-2-ylidene)[9] was initially designed according the following assumptions: (1) asymmetric coordination might differentiate the two Fe sites with respect to their redox activities upon one electron oxidation; (2) good donor ligands are needed for stabilization of the Fe^{II} oxidation state; and (3) sterically encumbering ligand substituents could potentially protect an open coordination site. A combination of PMe_3 and the N-heterocyclic carbene IMes fulfilled these requirements. The PMe_3 ligand has been used extensively in [FeFe]H_2ase active site synthetic analogues as a ligand that emulates the donor properties of the biological CN^-

(5) (a) Gloaguen, F.; Lawrence, J. D.; Rauchfuss, T. B. *J. Am. Chem. Soc.* **2001**, *123*, 9476–9477. (b) Chong, D.; Georgakaki, I. P.; Mejia-Rodriguez, R.; Sanabria-Chinchilla, J.; Soriaga, M. P.; Darensbourg, M. Y. *J. Chem. Soc., Dalton. Trans.* **2003**, *4158*, 4163. (c) Capon, J.-F.; Gloaguen, F.; Schollhammer, P.; Talarmin, J. *J. Electroanal. Chem.* **2004**, *566*, 241–247. (d) Jiang, S.; Liu, J.; Shi, Y.; Wang, Z.; Åkermark, B.; Sun, L. *Dalton Trans.* **2007**, 896–902. (e) Morvan, D.; Capon, J.-F.; Gloaguen, F.; Le Goff, A.; Marchivie, M.; Michaud, F.; Schollhammer, P.; Talarmin, J.; Yahouanc, J.-J.; Pichon, R.; Karvarec, N. *Organometallics* **2007**, *26*, 2042–2052. (f) Duan, L.; Wang, M.; Li, P.; Na, Y.; Wang, N.; Sun, L. *Dalton Trans.* **2007**, 1277–1283. (g) Mejia-Rodriguez, R.; Chong, D.; Reibenspies, J. H.; Soriaga, M. P.; Darensbourg, M. Y. *J. Am. Chem. Soc.* **2004**, *126*, 12004–12014. (h) Tye, J. W.; Lee, J.; Wang, H.-W.; Mejia-Rodriguez, R.; Reibenspies, J. H.; Hall, M. B.; Darensbourg, M. Y. *Inorg. Chem.* **2005**, *44*, 5550–5552.

(6) (a) Zhao, X.; Georgakaki, I. P.; Miller, M. L.; Mejia-Rodriguez, R.; Chiang, C.-Y.; Darensbourg, M. Y. *Inorg. Chem.* **2002**, *41*, 3917–3928. (b) Lemon, B. J.; Peters, J. W. *J. Am. Chem. Soc.* **2000**, *122*, 2793–3794.

(7) (a) Popescu, C. V.; Munck, E. *J. Am. Chem. Soc.* **1999**, *121*, 7877. (b) Nicolet, Y.; de Lacey, A. L.; Vernede, X.; Fernandez, V. M.; Hatchikian, E. C.; Fontecilla-Camps, J. C. *J. Am. Chem. Soc.* **2001**, *123*, 1596.

(8) Cao, Z.; Hall, M. B. *J. Am. Chem. Soc.* **2001**, *123*, 3734.

(9) Liu, T.; Darensbourg, M. Y. *J. Am. Chem. Soc.* **2007**, *129*, 7008–7009.

(10) Justice, A. K.; Rauchfuss, T. B.; Wilson, S. R. *Angew. Chem., Int. Ed.* **2007**, *46*, 6152.

(11) Tye, J. W.; Darensbourg, M. Y.; Hall, M. B. *Inorg. Chem.* **2006**, *45*, 1552–1559.

(12) Ezzaher, S.; Capon, J.-F.; Gloaguen, F.; Pétillon, F. Y.; Schollhammer, P.; Talarmin, J.; Pichon, R.; Kervarec, N. *Inorg. Chem.* **2007**, *46*, 3426–3428.

(13) Razavet, M.; Borg, S. J.; George, S. J.; Best, S. P.; Fairhurst, S. A.; Pickett, C. J. *Chem. Commun.* **2002**, 700.

ligand, without the complications of reactivity at the cyanide nitrogen. The IMes ligand is a strong σ-donor ligand with dynamic steric properties as a result of the low rotation barrier about the M−C bond in its metal complexes.[14] Thus, it was found that complex **1** displayed a reversible one-electron oxidation in its cyclic voltammogram and bulk chemical oxidation of **1** yielded $\mathbf{1_{ox}}$, (μ-pdt)(μ-CO)[Fe(CO)$_2$-PMe$_3$][Fe(CO)IMes]$^+$, which features ν(CO) IR and EPR spectroscopic properties and a core structure similar to that of the H_{ox} state of [FeFe]H_2ase. A density-functional theory (DFT) study indicated that the singly occupied molecular orbital (SOMO) is located on the IMes-bound Fe site, from which we could conclude an oxidation state assignment of (μ-pdt)(μ-CO)[Fe^{II}(CO)$_2$PMe$_3$][Fe^{I}(CO)IMes]$^+$.[15] Regioselective ^{13}CO incorporation into the NHC substituted side of $\mathbf{1_{ox}}$ was supportive of the assignment.[16]

Questions that arise from analysis of the $\mathbf{1_{ox}}$ model complex include (1) what steric role is played by the carbene's N-atom substitutents in protecting the open coordination site on the rotated Fe center; (2) what combination of steric/electronic factors and configurational isomers control the semibridging nature of the CO ligand; and (3) do these mixed valent synthetic analogues mimic the CO exchange reactivity of the H_{ox} state of the biological active site.

Herein, we present one electron oxidation chemistry of a series of asymmetrically disubstituted diiron complexes, (μ-pdt)[Fe^{I}(CO)$_2$PMe$_3$][Fe^{I}(CO)$_2$(NHC)], with a selection of N-heterocyclic carbene (NHC) ligands with different N-atom substituents. The questions posed above are addressed through a combination of experimental and computational approaches.

Experimental Section

Materials and Techniques. All reactions and operations were carried out on a double-manifold Schlenk vacuum line under N_2 or Ar atmosphere. Hexane, CH_2Cl_2, CH_3CN, toluene, and benzene were freshly purified on an MBraun Manual Solvent Purification System packed with Alcoa F200 activated alumina desiccant. The purified hexane, CH_2Cl_2, CH_3CN, and toluene were stored with molecular sieves under N_2 for no more than 1 week before experiments. THF was purified by distillation under N_2 from Na^0/benzophenone. The starting materials including (μ-pdt)[Fe(CO)$_3$]$_2$,[17] 1,3-bis(methyl)imidazolium iodide,[18] and 1-methyl,3-(2,4,6-trimethylphenyl)imidazolium iodide[19] were prepared according to literature procedures. Complexes **1** and $\mathbf{1_{ox}}$ were prepared as described previously.[9] The following materials were of reagent grade and were used as purchased from Sigma-Aldrich: $Fe_3(CO)_{12}$, 1,3-propanedithiol, 1,3-bis(2,4,6-trimethylphenyl)imidazolium chloride, trimethylphosphine, ferrocenium hexafluorophosphate, and cobaltocene.

All NMR spectra were measured on a Varian Mercury or Unity+ 300 MHz NMR spectrometer. ^{1}H NMR shifts are referenced to residual solvent resonances, according to literature values. ^{31}P NMR shifts are referenced to 100% H_3PO_4 (0 ppm). Solution IR spectra were recorded on a Bruker Tensor 27 FTIR spectrometer using 0.1 mm NaCl sealed cells. For thermally sensitive compounds (i.e., $\mathbf{1_{ox}}$, $\mathbf{2_{ox}}$, and $\mathbf{3_{ox}}$), solution spectra were recorded as rapidly as possible at room temperature (22 °C), minimizing the time the sample was warmed. X-band EPR spectra were recorded at 10 K on a Bruker EMX spectrometer using a Hewlett-Packard 5352B microwave frequency counter, a ER4102ST cavity, and an Oxford Instruments ESR900 cryostat.

Electrochemistry. Electrochemical measurements were conducted using a BAS 100A electrochemical analyzer. All voltammograms were obtained in a conventional, gastight three-electrode cell under an Ar atmosphere at 22 °C. The working electrode was a glassy carbon disk (0.071 cm^2) polished with 1 μm diamond paste and sonicated for 15 min prior to use. The supporting electrolyte was n-Bu_4NBF_4 (0.1 M in CH_3CN or CH_2Cl_2, as specified). For studies in CH_3CN as solvent, the reference electrode was Ag/Ag^+ prepared by immersing a silver wire in a CH_3CN solution of 0.01 M $AgNO_3$/0.1 M n-Bu_4NBF_4. For the CH_2Cl_2 studies, a silver wire anodized with AgCl was used. All potentials are reported relative to Fc^+/Fc as reference (Fc = Cp_2Fe). The counter electrode was platinum wire.

X-ray Structural Determination. For all reported structures a Bausch and Lomb 10 × microscope was used to identify suitable crystals of the same habit. Each crystal was coated in paratone, affixed to a Nylon loop and placed under streaming nitrogen (110 K) in a Bruker SMART 1000 CCD or Bruker-D8 Adv GADDS diffractometer (see details in Supporting Information,.cif file). The space groups were determined on the basis of systematic absences and intensity statistics. The structures were solved by direct methods and refined by full-matrix least-squares on F^2. Anisotropic displacement parameters were determined for all nonhydrogen atoms. Hydrogen atoms were placed at idealized positions and refined with fixed isotropic displacement parameters. Crystallographic data are listed in Supporting Information. The following is a list of programs were used: data collection and cell refinement, SMART WNT/2000 Version 5.632[20] or FRAMBO Version 4.1.05 (GADDS[21]); data reductions, SAINTPLUS Version 6.63;[22] absorption correction, SADABS;[23] structural solutions, SHELXS-97;[24] structural refinement, SHELXL-97;[25] graphics and publication materials, X-Seed Version 1.5.[26]

Theoretical Details. DFT calculations were performed using the B3LYP hybrid functional, the three parameter exchange functional of Becke (B3)[27] and the correlation functional of Lee, Yang, and Parr (LYP)[28] (B3LYP) as implemented in Gaussian 03.[29] The

(14) Doyle, M. J.; Lappert, M. F. *J. Chem. Soc., Chem. Commun.* **1974**, *17*, 679.
(15) Thomas, C. M.; Darensbourg, M. Y.; Hall, M. B. *J. Inorg. Biochem.* **2007**, *101*, 1752–1757.
(16) Thomas, C. M.; Liu, T.; Hall, M. B.; Darensbourg, M. Y. *Chem. Commun.* **2007**, 1563–1565.
(17) Lyon, E. J.; Georgakaki, I. P.; Reibenspies, J. H.; Darensbourg, M. Y. *J. Am. Chem. Soc.* **2001**, *123*, 3268–3278.
(18) Chu, Y.; Deng, H.; Cheng, J.-P. *J. Org. Chem.* **2007**, *72*, 7790–7793.
(19) Nieto-Oberhuber, C.; López, S.; Echavarren, A. M. *J. Am. Chem. Soc.* **2005**, *127*, 6178–6179.
(20) *SMART V5.632 Program for Data Collection on Area Detectors*; BRUKER AXS Inc.: Madison, WI
(21) *FRAMBO:FRAME Buffer Operation Version 41.05 Program for Data Collection on Area Detectors*; BRUKER AXS Inc.: Madison, WI.
(22) *SAINT V6.63 Program for Reduction of Area Detector Data*; BRUCKER AXS Inc.: Madison, WI.
(23) Sheldrick, G. M. *SADABS Program for Absorption Correction of Area Detector Frames*; Brucker AXS.: Madison, WI.
(24) Sheldrick, G. (1997) *SHELXS-97 Program for Crystal Structure Solution*; Institüt für Anorganische Chemie der Universität Göttingen: Göttingen, Germany.
(25) Sheldrick, G. (1997) *SHELXL-97 Program for Crystal Structure Refinement*; Institüt für Anorganische Chemie der Universität Göttingen: Göttingen, Germany.
(26) Barbour, L. J. *J. Supramol. Chem. 2001* **1999**, *1*, 189–191; "X-Seed-A software tool for supramolecular Crystallography".
(27) Becke, A. D. *J. Chem. Phys.* **1993**, *98*, 5648–5652.
(28) Lee, C.; Yang, W.; Parr, R. G. *Phys. Rev.* **1998**, *37*, 785–789.

effective core potentials and associated basis sets of Hay and Wadt (LANL2DZ)[30,31] were used on the iron, sulfur, and phosphorus atoms. For iron, the two outermost p functions were replaced by the reoptimized 4p functions as suggest by Couty and Hall.[32] For sulfur and phosphorus, the basis set was augmented by the d polarization function of Höllwarth et al.[33] All carbon, nitrogen, oxygen, and hydrogen atoms were represented using Dunning's double-ζ valence basis (D95).[34,35] For all calculated molecules discussed herein, the geometries were fully optimized and confirmed as minima by analytical frequency calculations at the same level of theory. For solvation calculations, single point calculations were performed at the same level of theory using the polarizable continuum model (PCM) and CH_2Cl_2 as the solvent. $\mathbf{3_{ox}}$ was also examined using both different density functionals and different basis sets to see if higher levels of theory led to better matches with the experimental structure, vibrational frequencies, and energy differences (see Supporting Information).

Synthetic Procedures. Note: Once isolated, the monosubstituted (μ-pdt)[Fe(CO)$_3$][Fe(CO)$_2$NHC] complexes ($\mathbf{1_{NHC}}$, $\mathbf{2_{NHC}}$, and $\mathbf{3_{NHC}}$) may be handled in air, as solutions of these complexes are reasonably air stable. The (μ-pdt)[Fe(CO)$_2$PMe$_3$][Fe(CO)$_2$NHC] complexes (**1**, **2**, and **3**) are more air sensitive, however, solids can be readily handled in air. The mixed valent (μ-pdt)[Fe(CO)$_2$PMe$_3$][Fe(CO)$_2$NHC]$^+$ complexes are highly sensitive to air and moisture. Air sensitive techniques were used throughout as a precautionary measure.

(μ-pdt)[Fe(CO)$_2$IMes][Fe(CO)$_3$] ($\mathbf{1_{NHC}}$) and (μ-pdt)[Fe(CO)$_2$IMe][Fe(CO)$_3$] ($\mathbf{3_{NHC}}$). Monosubstituted complexes, $\mathbf{1_{NHC}}$ and $\mathbf{3_{NHC}}$, were prepared in an alternate procedure from earlier reports.[5h,36] Solid (μ-pdt)[Fe(CO)$_3$]$_2$ (2.32 g, 6 mmol) and the imidazolium salt (6 mmol) were combined and dissolved in THF (50 mL). After stirring for 30 min, 12 mmol of KO^{t}Bu in 20 mL of THF was added, and the resulting mixture was stirred for an additional 30 min, monitoring by IR spectroscopy to confirm that the reaction had reached completion. Solid byproducts were removed from the reaction mixture by filtration through a sintered glass frit. After removal of THF from the filtrate under vacuum, the crude product was extracted into 50 mL ether, dried in vacuo, and then washed with methanol (2 × 10 mL). Yield: $\mathbf{1_{NHC}}$ (85%), $\mathbf{3_{NHC}}$ (83%).

(μ-pdt)[Fe(CO)$_2$IMesMe][Fe(CO)$_3$] ($\mathbf{2_{NHC}}$). Solid 1-methyl,3-(2,4,6-trimethylphenyl)imidazolium iodide (0.653 g, 2.00 mmol) was suspended in THF (50 mL). To this was added solid KO^{t}Bu (0.248 g, 2.21 mmol) and the resulting mixture was stirred for 2.5 h at 22 °C. To this cloudy yellow solution was added solid (μ-pdt)[Fe(CO)$_3$]$_2$) (0.771 g, 2.00 mmol). The solution immediately darkened to red/brown. After 2 h, the solution was filtered through Celite and dried in vacuo. The resulting red solids were dissolved in toluene and loaded onto a silica gel column (12 in × 1 in). Elution with petroleum ether removed excess starting material. The product was then eluted with 1:1 petroleum ether/THF. Solvent was evaporated from the dark red eluant to yield spectroscopically pure product (0.77 g, 69%). Crystals suitable for X-ray diffraction were grown via slow diffusion of Et_2O into a concentrated CH_2Cl_2 solution at −35 °C. IR (THF, cm^{-1}): 2035 (m), 2025 (m), 1970 (vs), 1949 (m), 1916 (w). ^{1}H NMR (300 MHz, acetone-d_6): δ = 7.65 (s, 1H, NCH), 7.27 (s, 1H, NCH), 7.05 (s, 2H, *m*-Mes), 4.16 (s, 3H, Me), 2.33 (s, 3H, *p*-Mes), 2.13 (m, 2H, pdt), 2.09 (s, 6H, *o*-Mes), 1.82 (m, 4H, pdt). Anal. Calcd for $C_{21}H_{22}N_2Fe_2S_2O_5$: C, 45.18; H, 3.97; N, 5.02. Found: C, 45.39; H, 4.50; N, 4.87.

(μ-pdt)[Fe(CO)$_2$IMesMe][Fe(CO)$_2$PMe$_3$] (2). To a stirred solution of $\mathbf{2_{NHC}}$ (0.226 g, 0.406 mmol) in toluene (25 mL) was added PMe_3 (0.21 mL, 2.0 mmol), followed by reflux for 16 h. The solution, devoid of starting material as monitored by IR, was filtered through a plug of silica gel, and volatiles were removed from the resulting dark red solution in vacuo to yield analytically pure product (0.144 g, 58%). IR (CH_2Cl_2, cm^{-1}): 1974 (m), 1934 (s), 1899 (m), 1884 (w). ^{1}H NMR (300 MHz, acetone-d_6): δ = 7.63 (s, 1H, NCH), 7.21 (s, 1H, NCH), 6.99 (s, 2H, *m*-Mes), 4.25 (s, 3H, Me), 2.31 (s, 3H, *p*-Mes), 2.07 (s, 6H, *o*-Mes), 1.75 (m, 4H, pdt), 1.51 (m, 2H, pdt), 1.37 (m, PMe_3). ^{31}P NMR (121 MHz, acetone-d_6): δ = 25.3 (s). ^{13}C NMR (300 MHz, CD_2Cl_2):): δ = 219 (CO at Fe2), 216 (d, J_{C-P} = 19 Hz, CO at Fe1). 193 (:C(NR$_2$)$_2$), 167 (Mes), 139 (Mes), 137 (Mes), 136 (Mes), 129 (Mes), 124 (NHC), 124 (NHC), 39 (Me), 30 (pdt), 25 (pdt), 21 (Mes), 20 (PMe_3), 18 (Mes). Anal. Calcd for $C_{23}H_{31}N_2Fe_2PS_2O_4$: C, 45.56; H, 5.15; N, 4.62. Found: C, 45.59; H, 5.02; N, 4.66.

(μ-pdt)[Fe(CO)$_2$IMe][Fe(CO)$_2$PMe$_3$] (3). The synthetic procedure is similar to that of **1** typically using ∼1 g of the $\mathbf{3_{NHC}}$ precursor. The reaction time is 24 h as indicated by in situ IR spectroscopy, and a different purification procedure was required. After the toluene reaction solution was filtered through Celite, removal of the volatiles from the filtrate in vacuo provided a dark red sticky residue. To the crude product was added methanol (5 mL) to solidify the product. The product was then collected as a solid on a sintered glass frit and washed with pentane (2 × 10 mL). Single crystals and samples for combustion analysis were obtained through crystallization in layered CH_2Cl_2/pentane. Yield: 60.0%. IR (CH_2Cl_2, cm^{-1}): 1974 (s), 1934 (s), 1898 (m), 1884 (m, sh). ^{1}H NMR (300 MHz, acetone-d_6): δ = 7.38 (s, 2H, NC*H*), 4.08 (s, 6H, N*Me*), 1.92 (t, 4H, pdt), 1.53 (br, 2H, pdt), 1.46 (d, PMe_3). ^{31}P NMR (121 MHz, acetone-d_6): δ = 29.5 (s). ^{13}C NMR (300 MHz, CD_2Cl_2): δ = 219 (CO at Fe−NHC), 216 (d, J_{C-P} = 19 Hz, CO at Fe−PMe_3). Anal. Calcd for $C_{23}H_{31}N_2Fe_2PS_2O_4$: C, 35.88; H, 4.62; N, 5.58. Found: C, 36.00; H, 4.80; N, 5.57.

{(μ-pdt)[Fe(CO)$_2$IMesMe][Fe(CO)$_2$PMe$_3$]}PF$_6^-$ ($\mathbf{2_{ox}}$). The synthetic procedure is similar to that published for $\mathbf{1_{ox}}$.[9] Solid (**2**) (0.035 g, 0.058 mmol) was dissolved in CH_2Cl_2 (25 mL) and cooled to −78 °C. While stirring, a solution of $FcPF_6$ (0.019 g, 0.058 mmol)

(29) Frisch, M. J.; Trucks, G. W.; Schlegel, H. B.; Scuseria, G. E.; Robb, M. A.; Cheeseman, J. R.; Montgomery, J. A., Jr.; Vreven, T.; Kudin, K. N.; Burant, J. C.; Millam, J. M.; Iyengar, S. S.; Tomasi, J.; Barone, V.; Mennucci, B.; Cossi, M.; Scalmani, G.; Rega, N.; Petersson, G. A.; Nakatsuji, H.; Hada, M.; Ehara, M.; Toyota, K.; Fukuda, R.; Hasegawa, J.; Ishida, M.; Nakajima, T.; Honda, Y.; Kitao, O.; Nakai, H.; Klene, M.; Li, X.; Knox, J. E.; Hratchian, H. P.; Cross, J. B.; Bakken, V.; Adamo, C.; Jaramillo, J.; Gomperts, R.; Stratmann, R. E.; Yazyev, O.; Austin, A. J.; Cammi, R.; Pomelli, C.; Ochterski, J. W.; Ayala, P. Y.; Morokuma, K.; Voth, G. A.; Salvador, P.; Dannenberg, J. J.; Zakrzewski, V. G.; Dapprich, S.; Daniels, A. D.; Strain, M. C.; Farkas, O.; Malick, D. K.; Rabuck, A. D.; Raghavachari, K.; Foresman, J. B.; Ortiz, J. V.; Cui, Q.; Baboul, A. G.; Clifford, S.; Cioslowski, J.; Stefanov, B. B.; Liu, G.; Liashenko, A.; Piskorz, P.; Komaromi, I.; Martin, R. L.; Fox, D. J.; Keith, T.; Al-Laham, M. A.; Peng, C. Y.; Nanayakkara, A.; Challacombe, M.; Gill, P. M. W.; Johnson, B.; Chen, W.; Wong, M. W.; Gonzalez, C.; Pople, J. A. *Gaussian 03*, Revision B.04; Gaussian, Inc.: Wallingford, CT, 2004.

(30) Hay, P. J.; Wadt, W. R. *J. Chem. Phys.* **1985**, *82*, 284–398.

(31) Hay, P. J.; Wadt, W. R. *J. Chem. Phys.* **1985**, *82*, 270–283.

(32) Couty, M.; Hall, M. B. *J. Comput. Chem.* **1996**, *17*, 1359–1370.

(33) Höllwarth, A.; Böhme, M.; Dapprich, S.; Ehlers, A. W.; Gobbi, A.; Jonas, V.; Köhler, K. F.; Stegmann, R.; Veldkamp, A.; Frenking, G. *Chem. Phys. Lett.* **1993**, *208*, 237–240.

(34) Dunning, Jr., T. H.; Hay, P. J. In *Methods of Electronic Structure Theory*; Schaefer H. F., III, Ed.; Plenum Press: New York, 1977; Vol. 3.

(35) Dunning, T. H., Jr. *J. Chem. Phys.* **1970**, *53*, 2823–2833.

(36) Capon, J.-F.; El Hassnaoui, S.; Gloaguen, F.; Schollhammer, P.; Talarmin, J. *Organometallics* **2005**, *24*, 2020–2022.

(37) Li, P.; Wang, M.; He, C.; Li, G.; Liu, X.; Chen, C.; Akermark, B.; Sun, L. *Eur. J. Inorg. Chem.* **2005**, *2506*, 2513.

(38) Lyon, E. J.; Georgakaki, I. P.; Reibenspies, J. H.; Darensbourg, M. Y. *Angew. Chem., Int. Ed.* **1999**, *38*, 3178–3180.

in CH_2Cl_2 (10 mL) was added dropwise. Upon addition, the solution darkened from red to burgundy, and IR spectroscopy revealed complete consumption of the starting material after ~20 min. Precooled hexane (20 mL) was added to precipitate the product, and the supernatant was removed with a cannula fitted with a PTFE membrane. The dark brown solid was washed successively by 5 mL of benzene and 5 mL of pentane to further remove impurities. The product was stored at −80 °C. IR (CH_2Cl_2, cm^{-1}): 2036(s), 2000 (vs), 1929 (w). μ_{eff} (Evans' method, CD_2Cl_2, 298 K): 1.87 μ_B. The thermal sensitivity of the product has thus far precluded elemental analysis.

{(μ-pdt)[$Fe^{II}(CO)_2$IMe][$Fe^{I}(CO)_2PMe_3$]}PF_6^- (3_{ox}). The preparation of $\mathbf{3_{ox}}$ followed a similar procedure as that described for $\mathbf{1_{ox}}$ and $\mathbf{2_{ox}}$.[9] At −78 °C under Ar, complex **3** (103.9 mg, 0.2 mmol) dissolved in CH_2Cl_2 (5 mL) was treated with a precooled solution of $FcPF_6$ (66.2 mg, 0.2 mmol) in 5 mL of CH_2Cl_2. The mixture was stirred at −78 °C for 0.5 h until in situ IR spectroscopy indicated there was no starting material remaining. Following precipitation with precooled hexanes (20 mL) and removal of the supernatant via filtration as described above, the dark brown crude product was washed successively by 5 mL of benzene and 5 mL of pentane. The product obtained was stored at −80 °C for further use. IR (CH_2Cl_2, cm^{-1}): 2036(s), 2005 (vs), 1981(s), 1929 (w). μ_{eff} (Evans' method, CD_2Cl_2, 298 K): 1.89 μ_B. The thermal sensitivity of the product has thus far precluded elemental analysis.

Generation of {(μ-pdt)(μ-CO)[$Fe^{I}(CO)_2$IMesMe][$Fe^{II}(CO)_2PMe_3$]}PF_6^-(2_{ox}-CO)and{(μ-pdt)(μ-CO)[$Fe^{I}(CO)_2$IMe][$Fe^{II}(CO)_2PMe_3$]}PF_6^-(3_{ox}-CO). At −78 °C, solutions of $\mathbf{2_{ox}}$ or $\mathbf{3_{ox}}$ (0.020 mmol) in CH_2Cl_2 were sparged with CO. The CO uptake was monitored by in situ solution IR spectroscopy.

Treatment of {(μ-pdt)(μ-CO)[Fe^{I}(CO)IMesMe][$Fe^{II}(CO)_2PMe_3$]}PF_6^- (2_{ox}) with ^{13}CO. A solution of $\mathbf{2_{ox}}$ (0.020 mmol) in 10 mL of CH_2Cl_2 was frozen with liquid N_2. The reaction flask was evacuated and refilled with 1 atm ^{13}CO. The temperature was raised to −78 °C, and the solution was magnetically stirred. The IR spectrum of the resulting reaction mixture was monitored by taking aliquots of this solution over the course of 1 h.

Results and Discussion

Spectroscopic Characterization of Complexes (μ-pdt)-[Fe(CO)$_2$NHC][Fe(CO)$_3$], $\mathbf{1_{NHC}}$-$\mathbf{3_{NHC}}$, and (μ-pdt)[Fe(CO)$_2$-NHC][Fe(CO)$_2$PMe$_3$], 1−3. The Fe^IFe^I precursors were synthesized via NHC ligand displacement of CO from (μ-pdt)[$Fe(CO)_3$]$_2$. Subsequent thermal substitution with PMe_3 ultimately led to product as deep red crystals as described in the Experimental Section and shown in Scheme 3. These complexes are at least moderately soluble in both nonpolar and polar organic solvents ranging from pentane to methanol. Solubility in polar solvents increases in the order of **1**, **2**, and **3**.

The FTIR data for the mono- and disubstituted complexes in the diatomic ligand region are listed in Table 1. In THF solution, the monosubstituted NHC complexes display similar IR patterns with five ν(CO) stretches at very similar frequencies. The second and third bands of $\mathbf{1_{NHC}}$ and $\mathbf{2_{NHC}}$ are well-defined while those of $\mathbf{3_{NHC}}$ significantly overlap. Very similar IR patterns and ν(CO) values were also observed for complexes **1**−**3**. The increased electron density at Fe with sequential CO substitution results in shifts of ν(CO) to lower values by 40 to 60 cm^{-1} compared to (μ-pdt)[$Fe(CO)_3$]$_2$ and (μ-pdt)[$Fe(CO)_3$][$Fe(CO)_2$NHC], respectively. The donating ability of NHC ligands compared to phosphine and CN^- ligands can be evaluated using ν(CO) IR stretches as an indicator of metal electrophilicity. The ν(CO) values of complexes $\mathbf{1_{NHC}}$−$\mathbf{3_{NHC}}$ are slightly lowered from those of (μ-pdt)[$Fe(CO)_3$][$Fe(CO)_2PMe_3$] but higher than that of (μ-pdt)[$Fe(CO)_3$][$Fe(CO)_2CN$]$^-$. A simple conclusion is that the electron-donating ability of the NHCs and PMe_3 are similar, and that both ligands create an environment about iron that is slightly less electron-rich than is that of the cyanide analogue.

Scheme 3

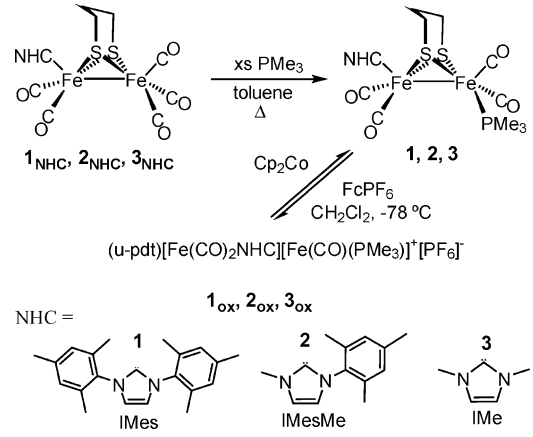

Cyclic Voltammetry of Complexes $\mathbf{1_{NHC}}$−$\mathbf{3_{NHC}}$ and 1−3. The redox behavior of the complexes was investigated using cyclic voltammetry (CV) for comparative purposes and to enable us to choose an appropriate chemical oxidant (and reductant) for solution redox chemistry (vide infra). Electrochemical data (referenced to Fc^+/Fc = 0.00 V)[39] are compared in Table 2 and assigned according to a previous report.[5,40] To explore the solvent effects on the different redox couples, especially the $Fe^{II}Fe^I/Fe^IFe^I$ couple of interest, CV measurements were performed in both coordinating (CH_3CN) and relatively noncoordinating solvent (CH_2Cl_2) for complexes **1**−**3.** The CV's of complexes **1**−**3** in CH_3CN (0.1 M [^{n}Bu$_4$N][BF_4], scan rate = 100 mV/s, 22 °C) display several redox events (Figure 1) that shift cathodically relative to those of $\mathbf{1_{NHC}}$, consistent with the increase in electron density at the diiron centers with the PMe_3/CO substitution. Under the conditions reported here, the cyclic voltammograms of all six complexes feature an irreversible reduction at negative potentials in CH_3CN (<−2 V vs Fc/Fc^+), with the disubstituted complexes **1**−**3** being more difficult to reduce by 0.2−0.5 V and at the limit of the solvent window.[41] From a detailed electrochemical investigation of 3_{NHC} by Capon et al. the conclusion was made that the reduction is a two-electron process and partially reversible.[40]

(39) In our measurements, the Fc+/Fc couple was recorded at 0.098 V vs AgNO3/Ag in CH3CN while lying at 0.244 V vs AgNO3/Ag in CH2Cl2.

(40) Capon, J.-F.; Ezzaher, S.; Gloaguen, F.; Petillion, F. Y.; Schollhammer, P.; Talarmin, J.; Davin, T. J.; McGrady, J. E.; Muir, K. W. *New J. Chem.* **2007**, *31*, 2052–2064.

(41) For complexes **2** and **3**, a small irreversible oxidation was observed at ca. −1.5 V. Regional scans indicate it can be attributed to the decomposition of reduced species; this feature is only present when potentials more negative than −2.0 V are applied.

Table 1. Infrared Spectroscopic Data For (μ-pdt)[Fe(CO)$_2$(L)]$_2$, Derivatives (reported in THF solution unless otherwise noted).

complex	υ(CO) (cm^{-1})	ref
(μ-pdt)[Fe(CO)$_3$]$_2$[a]	2074 (m), 2036 (vs), 1995 (s)	17
(μ-pdt)[Fe(CO)$_3$][Fe(CO)$_2$PMe$_3$][a]	2037 (s), 1980 (s), 1919 (m)	37
(μ-pdt)[Fe(CO)$_2$PMe$_3$]$_2$[a]	1979 (m), 1942 (s), 1898 (s)	6b
(μ-pdt)[Fe(CO)$_3$][Fe(CO)$_2$CN]$^-$	2027 (m), 1977 (s), 1944 (s), 1919 (m)	38
(μ-pdt)[Fe(CO)$_2$PMe$_3$] [Fe(CO)$_2$CN]$^-$	1971 (s), 1931 (s), 1895 (s), 1880 (sh)	38
(μ-pdt)[Fe(CO)$_3$][Fe(CO)$_2$IMes] (**1$_{NHC}$**)	2035(s), 2027(s), 1969(vs), 1947(m), 1916(m)	*b*
(μ-pdt)[Fe(CO)$_3$][Fe(CO)$_2$IMeM] (**2$_{NHC}$**)	2035 (s), 2025 (s), 1970 (vs), 1949(s), 1916(m)	*b*
(μ-pdt)[Fe(CO)$_3$][Fe(CO)$_2$IMe] (**3$_{NHC}$**)	2039 (s), 2031 (s), 1970(vs), 1950 (s), 1916 (m)	*b*
(μ-pdt)[Fe(CO)$_2$PMe$_3$][Fe(CO)$_2$IMes] (**1**)	1972 (s), 1933 (vs), 1897 (s), 1882 (m,sh)	*b*
(μ-pdt)[Fe(CO)$_2$PMe$_3$][Fe(CO)$_2$IMesMe] (**2**)	1974 (s), 1934 (s), 1899 (m), 1884 (m, sh)	*b*
(μ-pdt)[Fe(CO)$_2$PMe$_3$][Fe(CO)$_2$IMe] (**3**)	1974 (s), 1934 (s), 1898 (m), 1884 (m, sh)	*b*
{(μ-pdt)[Fe(CO)$_2$PMe$_3$][Fe(CO)$_2$IMes]}$^+$ (**1$_{ox}$**)	2037 (s), 1997 (vs), 1987 (s,sh), 1886 (w)	*b*
{(μ-pdt)[Fe(CO)$_2$PMe$_3$][Fe(CO)$_2$IMesMe]}$^+$ (**2$_{ox}$**)	2036(s), 2000 (vs), 1983(s, sh), 1929 (w)	*b*
{(μ-pdt)[Fe(CO)$_2$PMe$_3$][Fe(CO)$_2$IMes]}$^+$ (**3$_{ox}$**)	2036(s), 2005 (vs), 1981(s), 1929 (w)	*b*

[a] Spectrum recorded in acetonitrile; [b] Reported in this work.

Table 2. Electrochemical Potentials (V vs Fc$^+$/Fc) As Determined by Cyclic Voltammetry for (μ-pdt)[Fe(CO)$_2$(NHC)][Fe(CO)$_2$(L)] Complexes, **1$_{NHC}$**−**3$_{NHC}$** and **1**−**3** [a]

	CH$_3$CN			CH$_2$Cl$_2$		
complex	further oxidation(s)	Fe^{II}Fe^I/Fe^{I}Fe^I	Fe^{I}Fe^I/Fe^{I}Fe^0	further oxidation(s)	Fe^{II}Fe^I/Fe^{I}Fe^I	Fe^{I}Fe^I/Fe^{I}Fe^0
1$_{NHC}$	0.72	0.11	−2.10			
2$_{NHC}$	0.77	0.23	−2.12			
3$_{NHC}$		0.11	−2.01			
1	0.77, 0.14	−0.47	−2.36	0.85	−0.50	
2	0.70, −0.11	−0.33	−2.52	−0.12	−0.38	−2.50
3	0.84, 0.37	−0.24	−2.53	0.49	−0.33	

[a] Recorded in CH$_3$CN or CH$_2$Cl$_2$ with 0.1 M [^{n}Bu$_4$N][BF$_4$]; scan rate = 100 mV/s, 22 °C). The data for 3$_{NHC}$ was taken from ref 40.

In the presence of weak acid (HOAc), the current at the reduction potential of complex **1**−**3** increases with increasing concentrations of acid, indicative of electrocatalytic H$^+$ reduction by these diiron dithiolate models (see Supporting Information), as reported for **1$_{NHC}$**.[5h]

The cyclic voltammograms of both monosubstituted **1$_{NHC}$**−**3$_{NHC}$** and disubstituted **1**−**3** display irreversible oxidations at $E_{pa} \sim 0.7$ V. There is an additional oxidative process in all complexes, attributed to an Fe^{II}Fe^I/Fe^{I}Fe^I couple, which shows some reversibility and whose position depends on the degree of substitution, Table 2. The Fe^{II}Fe^I/Fe^{I}Fe^I couple ($E_{1/2}$ = −0.47 V) of complex **1** in CH$_3$CN was also observed in CH$_2$Cl$_2$ solution ($E_{1/2}$= −0.50 V) with a slight cathodic shift (Figure 1). The reversibility of this redox couple was well maintained at a slower scan rate (50 mV/s) in both solvents. The CV of complex **2** features a similar reversible Fe^{II}Fe^I/Fe^{I}Fe^I couple in both CH$_3$CN and CH$_2$Cl$_2$ solution, although this couple is shifted anodically by about 0.15 V from that of **1**. In contrast to complexes **1** and **2**, in CH$_3$CN solution, complex **3** shows a quasi-reversible Fe^{II}Fe^I/Fe^{I}Fe^I couple ($E_{1/2}$ = −0.24 V). In CH$_2$Cl$_2$, however, this process becomes fully reversible.[42] No additional events or changes in the Fe^{II}Fe^I/Fe^{I}Fe^I couple are observed when the CV's of complexes **1**−**3** are measured under a CO atmosphere rather than Ar.

Notably, the Fe^{II}Fe^I/Fe^{I}Fe^I couple of **1** occurs at a more negative potential than that of **2** or **3**, but the Fe^{I}Fe^I/Fe^{I}Fe^0 couple for **1** occurs at potentials more positive than that of **2** or **3**. As the IR data is convincing of the similar electron-donating ability of the three NHC ligands, this difference in redox potentials of **1** versus **2** and **3** must be ascribed to the steric differences in the ligands. The steric control of such a thermodynamic property may be a result of stabilization of the rotated forms or of different configurational/conformational isomers, as explored below by DFT calculations. Note that complex **2** which has the possibility of rotational isomers of the NHC shows yet another oxidative event, at about 0.1 V, which could reflect the presence of another stable form.

Synthesis and Spectroscopic Characterization of Complex 1$_{ox}$−**3$_{ox}$.** On the basis of the electrochemical data regarding the Fe^{II}Fe^I/Fe^{I}Fe^I couple of complexes **1**−**3**, we performed one electron oxidation at −78 °C following the procedure described in our previous communication, with subsequent back-reduction to confirm reversibility.[9] In CH$_2$Cl$_2$, oxidation of the red Fe^{I}Fe^I complexes **1**−**3** with 1 equiv of FcPF$_6$ generated the corresponding brown Fe^{II}Fe^I complexes, **1$_{ox}$**, **2$_{ox}$**, and **3$_{ox}$** within 0.5 h (Figure 2). Monitoring by IR spectroscopy indicates that the oxidized species could be returned to their respective Fe^{I}Fe^I forms by reduction with Cp$_2$Co at −78 °C. The thermal stability of the oxidized complexes decreases with decreasing steric bulk of the NHC ligand (**1$_{ox}$** > **2$_{ox}$** > **3$_{ox}$**). Thus, while **1$_{ox}$** is modestly stable in solution at room temperature for short time periods, appreciable decomposition of **2$_{ox}$** and **3$_{ox}$** occurs within minutes at room temperature, and solutions of these complexes must be stored at −40 °C or below.

It is noteworthy that the Fe^{II}Fe^I mixed valent species observed in this work and in that of Justice et al. requires the use of a noncoordinating solvent.[10] When CH$_3$CN or THF is used, the mixed valent species is not observed by IR

(42) It should be noted that, for voltammetric measurements of complex **3** in CH$_2$Cl$_2$, multiple scans could be applied to the Fe^{II}Fe^I/Fe^{I}Fe^I couple within the range of ca. 0.2 to −0.8 V while the whole CV could not be reproduced after one full scan. This is tentatively attributed to some form of radical promoted degradation that the complex undergoes in the electrochemical cell at very negative or very positive potentials. Complexes **1** and **2** showed similar phenomena but with better tolerance.

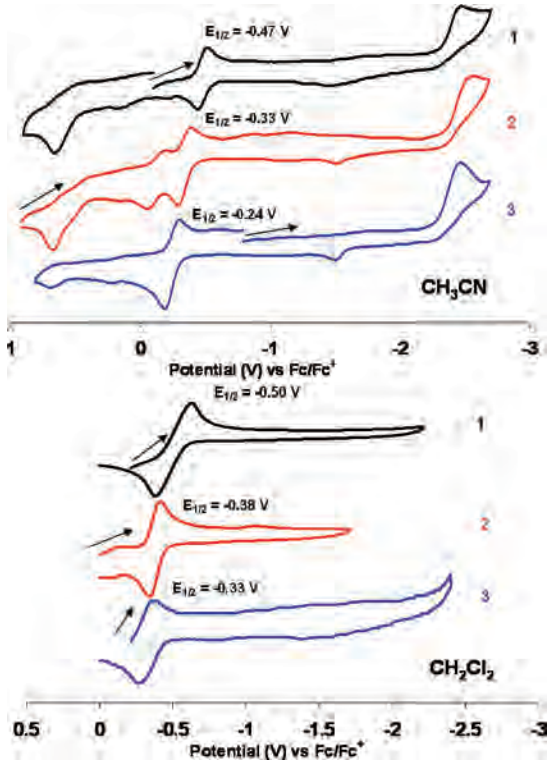

Figure 1. Cyclic voltammograms of (μ-pdt)[Fe(CO)$_2$PMe$_3$][Fe(CO)$_2$IMes] (**1**, black), (μ-pdt)[Fe(CO)$_2$PMe$_3$][Fe(CO)$_2$IMesMe] (**2**, red), and (μ-pdt)[Fe(CO)$_2$PMe$_3$][Fe(CO)$_2$IMe] (**3**, blue) in CH_3CN (top) and CH_2Cl_2 (bottom). All potentials are reported vs Fc^+/Fc (0.1 M [^{n}Bu$_4$N][BF$_4$], scan rate = 100 mV/s, 22 °C).

spectroscopy. Presumably coordinating solvents promote disproportionation yielding $Fe^{II}Fe^{II}$ species, consistent with the observations of Rauchfuss et al., in which the solvent-coordinated diferrous species (μ-SCH$_2$CH$_2$S)(μ-CO)[Fe(CO)$_2$-(PMe$_3$)][Fe(dppv)(solv)]$^{2+}$ (solv = CH_3CN or $(CH_3)_2C{=}O$) was isolated from the addition of 2 equiv of Fc^+ to the Fe^IFe^I dithiolate precursor (μ-edt)[Fe(CO)$_2$(PMe$_3$)[Fe(CO)(dppv)] (dppv = 1,2-(diphenylphosphino)vinylidene).[4d]

Complexes $\mathbf{1_{ox}}$−$\mathbf{3_{ox}}$ display quite different IR spectra from those of their reduced precursors with a blue shift of about 40∼60 cm^{-1}, consistent with the formation of more electron-deficient species (Figure 2). Within this series of mixed valent $Fe^{II}Fe^I$ complexes, several observations concerning their IR spectra can be summarized by the following: (i) The highest energy band of the series occurs at almost identical frequency around 2036 cm^{-1}. (ii) Overlap of the second and the third band decreases in the order of $\mathbf{1_{ox}}$ (1997 (vs), 1987 (s,sh)), $\mathbf{2_{ox}}$ (2000 (vs), 1983(s, sh)), and $\mathbf{3_{ox}}$ (2005 (vs), 1981(s)). (iii) The fourth band of $\mathbf{1_{ox}}$ (1861 (w)), indicative of a semibridging CO, lies at a much lower frequency relative to the value of 1929 (w) cm^{-1} for $\mathbf{2_{ox}}$ and $\mathbf{3_{ox}}$. This suggests that in the latter two complexes there is either no μ-CO or the extent of bridging character is greatly diminished in comparison to $\mathbf{1_{ox}}$. (iv) In the case of $\mathbf{2_{ox}}$, the absorption intensity of the lowest energy CO vibration is much smaller than those of complexes $\mathbf{1_{ox}}$ and $\mathbf{3_{ox}}$.

Complex $\mathbf{1_{ox}}$ was also identified by electrospray ionization mass spectrometry (ESI-MS); the mass spectrum of $\mathbf{1_{ox}}$ features an isotope pattern for the parent cation at m/z = 710, as well as several species resulting from CO loss (see

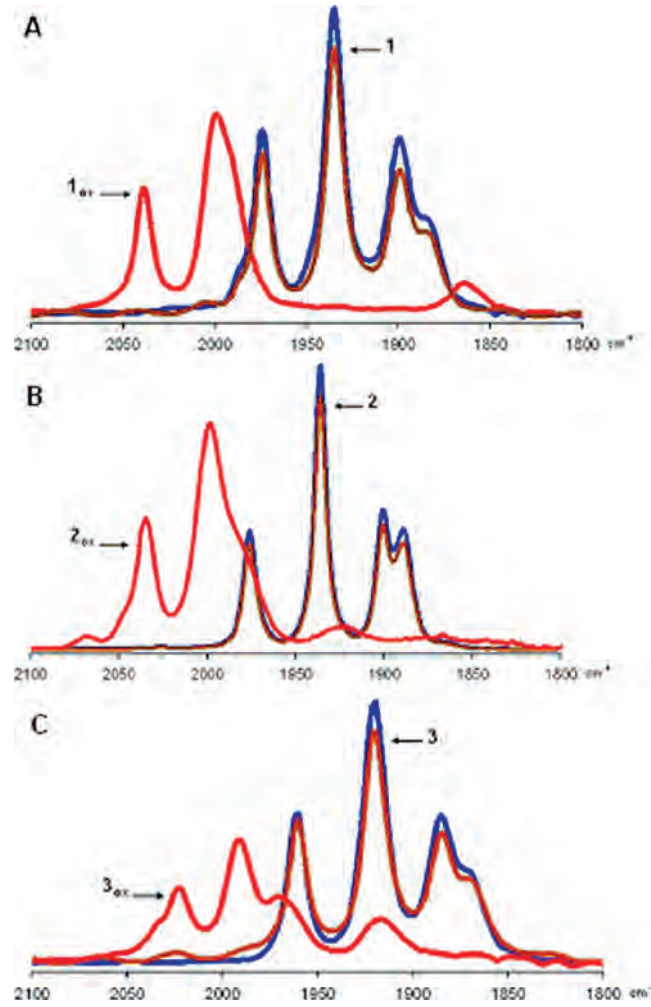

Figure 2. Solution IR spectra (CH_2Cl_2) showing the reversibility of the one-electron oxidation of **1**(A), **2** (B), and **3** (C). Blue IR spectrum: neutral **1**, **2**, and **3**; Red IR spectrum: cationic $\mathbf{1_{ox}}$, $\mathbf{2_{ox}}$, and $\mathbf{3_{ox}}$ generated by treatment of **1**, **2**, and **3**, respectively, with $FcPF_6$ in CH_2Cl_2 at −78 °C; Brown IR spectrum: neutral **1**, **2**, and **3** regenerated by addition of $CoCp_2$ (or $CoCp^*_2$) to $\mathbf{1_{ox}}$, $\mathbf{2_{ox}}$, and $\mathbf{3_{ox}}$, respectively, in CH_2Cl_2 at −78 °C.

Supporting Information). However, because of their thermal instability, $\mathbf{2_{ox}}$ and $\mathbf{3_{ox}}$ could not be detected by using the same technique.

The solution magnetic moments of complexes $\mathbf{1_{ox}}$−$\mathbf{3_{ox}}$, determined by using the Evans method,[43] were found to be 1.86, 1.87, and 1.89 μ_B, respectively, consistent with $S = {}^1/_2$ species. As expected, all three compounds are EPR active, as shown in the X-band EPR spectra given in Figure 3. The EPR spectrum of complex $\mathbf{1_{ox}}$ features a well-defined rhombic signal with g values similar to that of the H_{ox} state of [FeFe]H$_2$ase (simulated values for $\mathbf{1_{ox}}$: g_1 = 2.099, g_2 = 2.022, g_3 = 2.007; values reported for H_{ox}: 2.10, 2.04, 1.99).[44] In contrast, the EPR spectra of complexes $\mathbf{2_{ox}}$ (g_1 = 2.095, g_2 = 2.045, g_3 = 2.014) and $\mathbf{3_{ox}}$ (g_1 = 2.104, g_2 = 2.053, g_3 = 2.017) feature broader, more axial signals, indicating that the unpaired electron in these complexes is in a more symmetrical environment. Note that simulation of these EPR spectra did not require any ^{31}P superhyperfine coupling interactions.

Molecular Structures. Crystals of $\mathbf{2_{NHC}}$, **2**, and **3** suitable for crystallographic analysis were grown as described in the

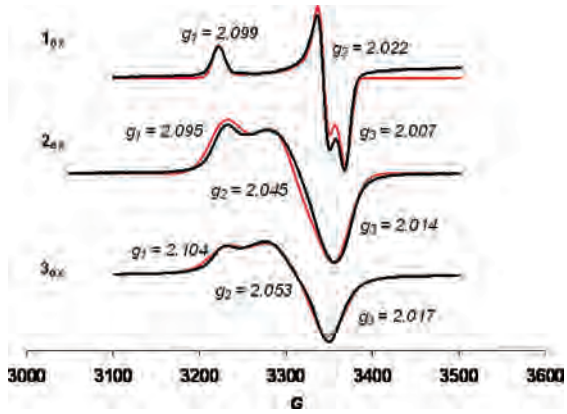

Figure 3. Experimental (black) and simulated (red) EPR spectra of $\mathbf{1_{ox}}$ (top), $\mathbf{2_{ox}}$ (middle), and $\mathbf{3_{ox}}$ (bottom). Spectra were recorded in frozen CH_2Cl_2 at 10 K, X band. Simulation parameters: $\mathbf{1_{ox}}$: $g_1 = 2.099$ (line width = 13 G), $g_2 = 2.022$ (line width = 11 G), $g_3 = 2.007$ (line width = 13 G); $\mathbf{2_{ox}}$: $g_1 = 2.095$ (line width = 35 G), $g_2 = 2.045$ (line width = 43 G), $g_3 = 2.014$ (line width = 33 G); $\mathbf{3_{ox}}$: $g_1 = 2.104$ (line width = 40 G), $g_2 = 2.053$ (line width = 45 G), $g_3 = 2.017$ (line width = 30 G).

Experimental Section. The structures of **1** and $\mathbf{1_{ox}}$ were reported in a previous communication.[9] Selected structural parameters for **1** and $\mathbf{1_{ox}}$ along with the new structures are listed in Table 3. For clarity, ball and stick drawings are used to represent all conformers as determined by solid state X-ray diffraction (Figure 4). All of the neutral Fe^IFe^I complexes share a butterfly diiron core in which each iron adopts a square pyramidal geometry. As a general structural feature, the NHC ligand coordinates in the apical position while a basal site is preferred for additional ligand substitution with phosphines in the disubstituted complexes **1**−**3**. This orientation of the NHC ligand likely minimizes steric interactions of the NHC substituents with the rest of the iron coordination environment. In the solid state, the bridgehead methylene group of the pdt bridge points toward the NHC-coordinated Fe site, except in the case of complex **3**. In both the mono- and disubstituted series, the Fe(2)−C(11) bond distance increases with the size of the NHC ligand substituents and undergoes little change upon PMe_3 addition. All of the Fe^IFe^I complexes presented in this study have similar Fe−Fe distances ranging from 2.527 Å to 2.557 Å, typical for Fe^IFe^I diiron dithiolates.

As previously reported,[9] the solid state structure of $\mathbf{1_{ox}}$ (Figure 5) confirms that upon one electron oxidation, the ligands about the IMes-coordinated iron (Fe(2)) center reconfigures such that a terminal CO ligand occupies the area under the Fe−Fe vector to form a semibridging CO. This semibridging character is evident from the asymmetric Fe−C distances, with a Fe(1)−C(3) distance of 2.196 Å, and the Fe(2)−C(3) distance of 1.864 Å is significantly elongated from that of the terminal COs (Fe(1)−C(1) = 1.808 Å, Fe(1)−C(2) = 1.782, Fe(2)−C(4) = 1.795 Å). Interestingly, the plane of the IMes ligand also twists to a large extent (~90°), which is likely to reduce steric interactions with the surrounding CO ligands. Overall, the structural features of $\mathbf{1_{ox}}$ bear remarkable resemblance to the H_{ox} state of [FeFe]H_2ase. In the case of $\mathbf{1_{ox}}$, both IMes and PMe_3 can be thought of as CN^- mimics on the distal (Fe_d) and proximal (Fe_p) iron sites, respectively. The Fe(2) of $\mathbf{1_{ox}}$, which has a five-coordinate environment and an open site, can be compared to Fe_d in H_{ox} while the Fe(1) of $\mathbf{1_{ox}}$ can be considered as Fe_p of the enzymatic system, with a CO ligand in place of the cysteinyl sulfur. Unfortunately, after many frustrating attempts, complexes $\mathbf{2_{ox}}$ and $\mathbf{3_{ox}}$ could not be crystallized; thus, DFT calculations (vide infra) were undertaken to guide our understanding of the geometries of $\mathbf{2_{ox}}$ and $\mathbf{3_{ox}}$.

Despite the formal loss of a full Fe−Fe bond as compared to its Fe^IFe^I precursor, $\mathbf{1_{ox}}$ shows only a minor lengthening of its Fe−Fe distance (2.553(2) Å for **1** vs 2.566(1) Å for $\mathbf{1_{ox}}$). In the case of previously reported $Fe^{II}Fe^{II}$ species, the value is around 2.57 Å for $Fe^{II}Fe^{II}(\mu$-H) hydride models and about 2.55 Å for $Fe^{II}Fe^{II}(\mu$-CO).[4d,e] The similar Fe−Fe distances conserved in all three oxidation states can be rationalized by the close interactions of each Fe center with the bridging ligands, the sulfur of the dithiolate, as well as the bridging H or CO.

Reactivities of Complexes $\mathbf{1_{ox}}$, $\mathbf{2_{ox}}$, and $\mathbf{3_{ox}}$ Toward Extrinsic CO: CO Uptake and ^{13}CO Exchange. Consistent with the known reversible inhibition of H_2 oxidation activity by carbon monoxide in [FeFe]H_2ase,[45] IR spectroscopy and X-ray crystallography have shown that extrinsic CO binds to the open coordination site on the Fe_d center generating the so-called H_{ox}^{CO} form of the enzyme.[44,46] In a revisitation of earlier IR studies, Roseboom et al. found that, in the absence of light at 2 °C, ^{13}CO binds to the open site on Fe_d and, under these conditions, does not exchange with the intrinsic CO ligands.[47] Upon illumination at room temperature, however, the ^{13}CO regioselectively exchanges specifically with the CO ligands on Fe_d, as shown in Scheme 4. Because our overall characterization of complex $\mathbf{1_{ox}}$ indicated that it bears similar structural, magnetic, and electronic features to the enzymatic H_{ox} state, we have explored the CO binding affinity and ^{13}CO exchange ability of $\mathbf{1_{ox}}$, $\mathbf{2_{ox}}$, and $\mathbf{3_{ox}}$. The experiments described below are interpreted based on assignments of CO stretching modes according to Figure 6.

When a CH_2Cl_2 solution of $\mathbf{1_{ox}}$ (generated in situ) is sparged with CO at −78 °C for 90 min, changes in the ν(CO) region of the IR spectrum occur as shown in Figure 7A. The growth of a new ν(CO) band at 2021 cm^{-1} is accompanied by an increase in intensity of the band(s) centered at ~1997 cm^{-1}. However, the band at 1861 cm^{-1}, assigned to the bridging CO, undergoes little change. This apparent CO

(43) Evans, D. F. *J. Chem. Soc.* **1959**, 2003.
(44) Albracht, S. P. J.; Roseboom, W.; Hatchikian, E. C. *J. Biol. Inorg. Chem.* **2006**, *11*, 88–101.
(45) (a) Thauer, R. K.; Kaufer, B.; Zahringer, M.; Jungermann, K. *Eur. J. Biochem.* **1974**, *42*, 447. (b) Erbes, D. L.; Burris, R. H. *Biochim. Biophys. Acta* **1978**, *525*, 45. (c) Adams, M. W. *J. Biol. Chem.* **1987**, *262*, 15054. (d) Kowal, A. T.; Adams, M. W.; Johnson, M. K. *J. Biol. Chem.* **1989**, *264*, 4342. (e) Patil, D. S.; Huynh, B. H.; He, S. H.; Peck, H. D.; Dervartanian, D. V.; Legall, J. *J. Am. Chem. Soc.* **1988**, *110*, 8533–8534.
(46) (a) Lemon, B. J.; Peters, J. W. *Biochemistry* **1999**, *38*, 12969–12973. (b) Lemon, B. J.; Peters, J. W. *J. Am. Chem. Soc.* **2000**, *122*, 2793–3794. (c) Silakov, A.; Reijerse, E. J.; Albracht, S. P. J.; Hatchikian, E. C.; Lubitz, W. *J. Am. Chem. Soc.* **2007**, *129*, 11447–11458. (d) Pierik, A. J.; Hulstein, M.; Hagen, W. R.; Albracht, S. P. J. *Eur. J. Biochem.* **1998**, *258*, 572–578.

Table 3. Selected Interatomic Distances (Å) and Angles (deg) for $\mathbf{2_{NHC}}$, **1**, **2**, **3**, and $\mathbf{1_{ox}}$

	$\mathbf{2_{NHC}}$	**1**	**2**	**3**	$\mathbf{1_{ox}}$
Fe(1)−Fe(2)	2.527(1)	2.553(2)	2.557(8)	2.55(1)	2.566(1)
Fe(1)−P(1)		2.225(3)	2.20(1)	2.212(2)	2.268(2)
Fe(2)−C(11)	1.971(3)	2.013(1)	1.980(4)	1.971(6)	2.000(4)
Fe(1)−C(3)					2.194(4)
Fe(2)−C(3)	1.774(3)	1.740(1)	1.765(5)	1.748(6)	1.864(4)
Fe(2)−S(1)	2.2807(9)	2.276(3)	2.262(1)	2.281(2)	2.299(2)
Fe(2)−S(2)	2.277(1)	2.295(3)	2.274(1)	2.271(2)	2.282(1)
S(1)−Fe(2)−C(11)	104.89(8)	105.2(3)	100.0(1)	100.7(2)	160.9(1)
S(2)−Fe(2)−C(11)	105.90(8)	106.9(3)	101.2(1)	110.5(2)	92.3(1)
Fe(1)−S(1)−Fe(2)	67.52(3)	68.4(1)	68.95(3)	68.16(5)	68.2(3)
Fe(1)−C(3)−Fe(2)					77.9(1)
Fe(1)−C(3)−O(3)					129.8(3)
Fe(2)−C(3)−O(3)					151.9(3)

Scheme 4

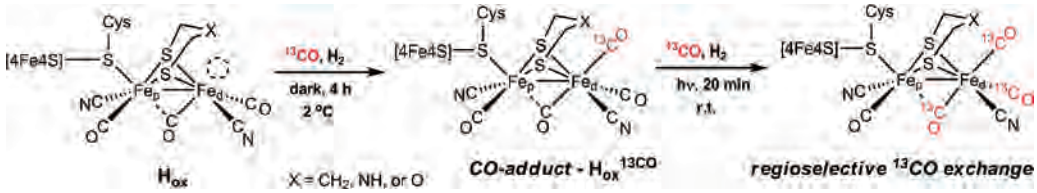

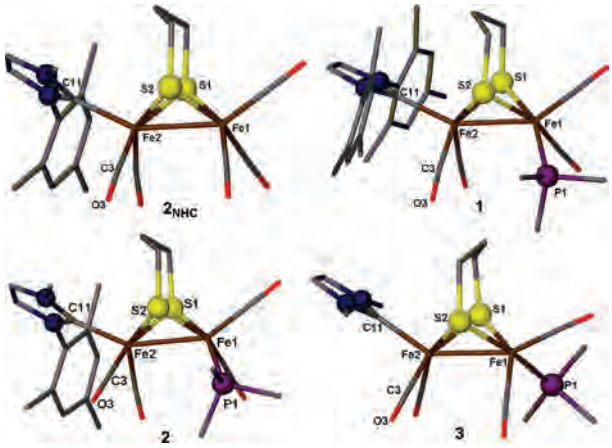

Figure 4. Solid state molecular structures (ball and stick representation) of complexes $\mathbf{2_{NHC}}$, **1**, **2**, and **3**.

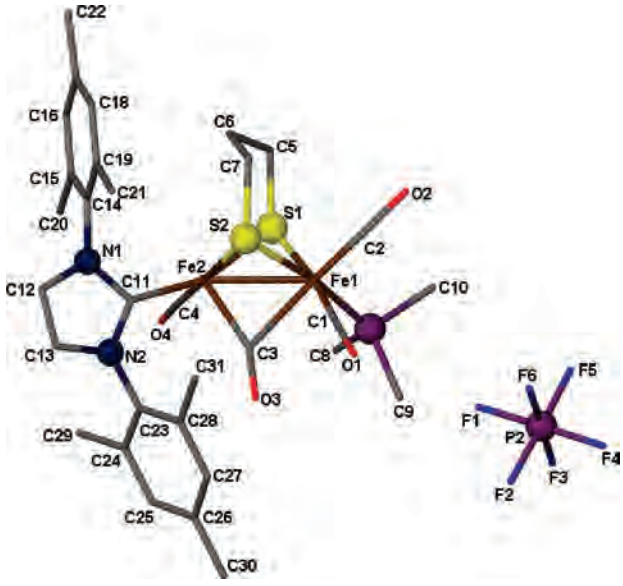

Figure 5. Solid state molecular structure (ball and stick representation) of $\mathbf{1_{ox}}$.[9]

binding process is at equilibrium as it does not proceed upon further exposure to CO; its reversibility is indicated by the fact that the original spectrum of $\mathbf{1_{ox}}$ is reclaimed on evacuation or on bubbling the solution containing $\mathbf{1_{ox}}^{CO}$ with N_2 or Ar.

In contrast, the reactions of complexes $\mathbf{2_{ox}}$ and $\mathbf{3_{ox}}$ with CO at −78 °C proceed to completion within 30 min (Figure 7B,C). For both complexes, new bands at 2021 and 1996 cm^{-1} are clearly identified in their respective IR spectra, attributed to formation of the CO-adducts $\mathbf{2_{ox}}^{CO}$ and $\mathbf{3_{ox}}^{CO}$. The reversibility of this process was established by recovery of the original IR spectra of $\mathbf{2_{ox}}$ and $\mathbf{3_{ox}}$ upon purging a solution of $\mathbf{2_{ox}}^{CO}$ or $\mathbf{3_{ox}}^{CO}$ with Ar or N_2 or by exposure of these solutions to vacuum. The greater thermal stability of $\mathbf{2_{ox}}^{CO}$ and $\mathbf{3_{ox}}^{CO}$ over $\mathbf{1_{ox}}^{CO}$ is indicated by a much slower rate of CO release by the less sterically congested derivatives. Interestingly, the positions of the lowest energy CO stretches at 1929 cm^{-1} for $\mathbf{2_{ox}}$ and $\mathbf{3_{ox}}$ are retained in $\mathbf{2_{ox}}^{CO}$ and $\mathbf{3_{ox}}^{CO}$ but appear to diminish in intensity relative to the other IR features. We have been unable to characterize $\mathbf{2_{ox}}^{CO}$ and $\mathbf{3_{ox}}^{CO}$ in the solid state by X-ray diffraction, but on the basis of calculations using DFT calculations (vide infra), we propose

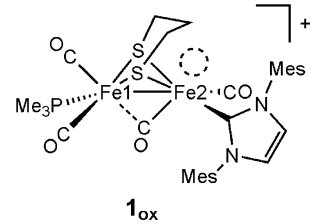

$\mathbf{1_{ox}}$

υ(CO)	assignment
2036 cm^{-1}	υ_{sym} Fe1(CO)$_2$
1998 cm^{-1}	υ Fe2(CO)$_{terminal}$
1985 cm^{-1}	υ_{asym} Fe1(CO)$_2$
1861 cm^{-1}	υ Fe2(CO)$_{bridging}$

Figure 6. Assignment of IR CO stretches for complex $\mathbf{1_{ox}}$.

that $\mathbf{2}_{ox}$ and $\mathbf{3}_{ox}$ undergo CO uptake at the open site on the rotated Fe center, as in H_{ox}^{CO}. A CO adduct is also observed by Rauchfuss et al. upon addition of extrinsic CO to (μ-SCH_2CH_2S)[$Fe(CO)_2(PMe_3)$][$Fe(CO)(dppv)$]$^+$.[48] As the CO binding site is presumed to be the Fe^I center, containing electron density at the "open" site as in $\mathbf{1}_{ox}$,[15] the binding of CO should result in substantial electron reorganization. This is supported by EPR spectroscopy on the exogeneous CO adducts, as described below.

The low temperature EPR spectrum (X-band, CH_2Cl_2, 10 K) of $\mathbf{2}_{ox}^{CO}$ (Figure 8) is distinct from that of its precursor, $\mathbf{2}_{ox}$. Indicated by simulation to be due to a single species, the EPR spectrum of $\mathbf{2}_{ox}^{CO}$ features a rhombic signal with $g_1 = 2.093$, $g_2 = 2.036$, $g_3 = 2.002$. In addition to the difference in g values between $\mathbf{2}_{ox}$ and $\mathbf{2}_{ox}^{CO}$, the EPR spectrum of $\mathbf{2}_{ox}^{CO}$ is best simulated with superhyperfine coupling to ^{31}P (spin = $^1/_2$) in g_3 ($A = 140$ MHz), a coupling which is not seen in the spectrum of $\mathbf{2}_{ox}$. This implies that CO binding leads to significant delocalization of the unpaired electron onto both the NHC and PMe_3-ligated iron atoms, as also predicted by computations (vide infra). Interestingly, electrochemical interrogation of $\mathbf{2}_{ox}^{CO}$ reveals substantially different redox properties from its unsubstituted congener $\mathbf{2}_{ox}$. Unlike $\mathbf{2}_{ox}$, cyclic voltammetry data indicates that $\mathbf{2}_{ox}^{CO}$ cannot be easily reduced to the Fe^IFe^I oxidation state (no reductive events were observed within the solvent window of CH_2Cl_2, see Supporting Information).

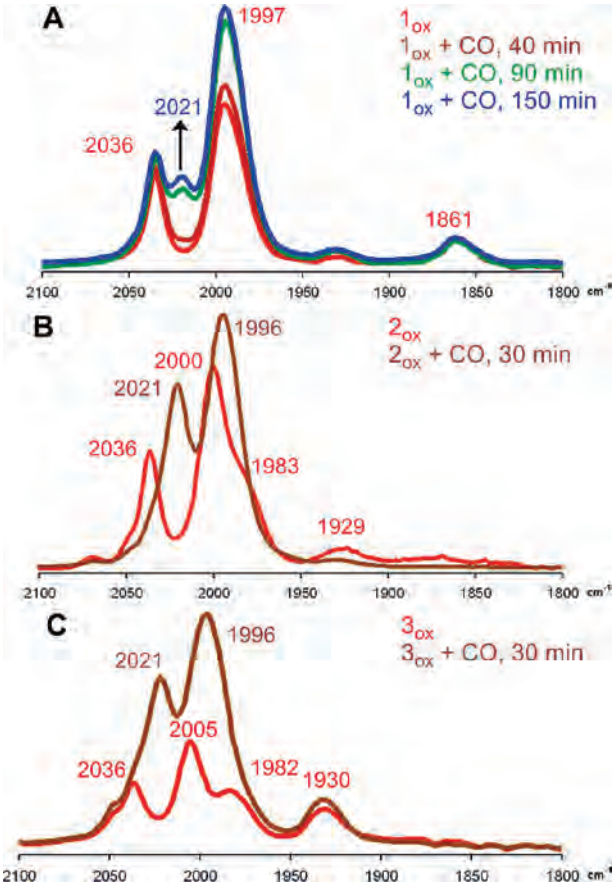

Figure 7. Infrared spectra (recorded at ca. 22 °C) of CH_2Cl_2 solutions of $\mathbf{1}_{ox}$(A), $\mathbf{2}_{ox}$ (B),and $\mathbf{3}_{ox}$(C) following CO sparging at −78 °C.

Despite the reluctance of $\mathbf{1}_{ox}$ to form a stable $\mathbf{1}_{ox}^{CO}$ adduct, we reported in a prior communication of preliminary results that isotopic exchange with extrinsic ^{13}CO occurs readily, mimicking the $^{13}CO/^{12}CO$ exchange activity of H_{ox} under certain conditions.[16] Under a blanket of ^{13}CO (1 atm) at −78 °C in CH_2Cl_2 in the absence of light, $\mathbf{1}_{ox}$ undergoes exchange with ^{13}CO exclusively into the semibridging and terminal CO positions on the IMes-substituted, paramagnetic Fe^I center. This regioselective $^{13}CO/^{12}CO$ exchange was observed by IR spectroscopy on the paramagnetic $\mathbf{1}_{ox}$ and by ^{13}C NMR spectroscopy on the reduced, ^{13}CO-labeled product $\mathbf{1}$.[16] At room temperature, however, the extrinsic ^{13}CO scrambles into all positions of $\mathbf{1}_{ox}$. A proposed mechanism for the regioselective isotopic exchange is presented in Scheme 5. In this path, ^{13}CO transiently binds to the open coordination site of $\mathbf{1}_{ox}$. Rotation about the Fe center with concomitant dissociation of a CO ligand restores the original geometry of $\mathbf{1}_{ox}$ but with a labeled ^{13}CO ligand. Repetition of this ^{13}CO binding/^{12}CO loss process generates the regioselectively labeled $\mathbf{1}_{ox}$ following path **A** in Scheme 5. Subsequent warm-up to 22° leads to scrambling throughout $\mathbf{1}_{ox}$.

To determine whether the spectroscopic and CO binding ability differences between $\mathbf{1}_{ox}$ and its less sterically encumbered derivatives, $\mathbf{2}_{ox}$ and $\mathbf{3}_{ox}$, might result in different ^{13}CO exchange behavior, the reactivity of $\mathbf{2}_{ox}$ with extrinsic ^{13}CO was investigated. Interpretation of the spectral data was complicated by the ability of $\mathbf{2}_{ox}$ to more easily form a CO adduct leading to possible ^{13}CO exchange into two species, $\mathbf{2}_{ox}$ and $\mathbf{2}_{ox}^{CO}$. The presence of 1 atm of ^{13}CO at −78 °C (i.e., without sparging), in the dark, results in immediate changes in the IR spectrum of $\mathbf{2}_{ox}$ (Figure 9). After 10 min, new CO stretches appear at 2029, 1973, 1958, and 1890 cm^{-1} while the bands at 2037, 2000 and 1929 cm^{-1} diminish in intensity. Over the course of 1 h, the new bands continue to increase in intensity while those corresponding to the starting material decrease. As the reaction procedes, the relative intensity of the band at 1958 cm^{-1} increases with respect to that at 1973 cm^{-1}, indicating that these IR bands correspond to two different species. On the basis of the change in reduced mass, complete exchange of ^{13}CO into all positions of $\mathbf{2}_{ox}$ should result in an IR spectrum with bands at 1993

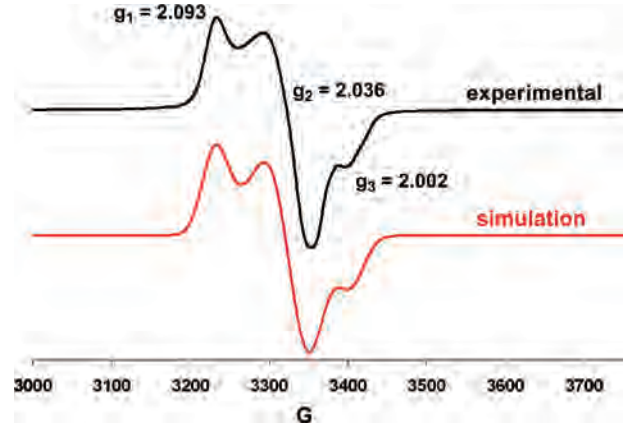

Figure 8. Experimental (top) and simulated (bottom) EPR spectrum of $\mathbf{2}_{ox}^{CO}$ (in CH_2Cl_2 at 10 K, X band). Simulation parameters: $g_1 = 2.093$ (line width = 32 G), $g_2 = 2.036$ (line width = 44 G), $g_3 = 2.002$ (line width = 35 G, $A = 140$ MHz).

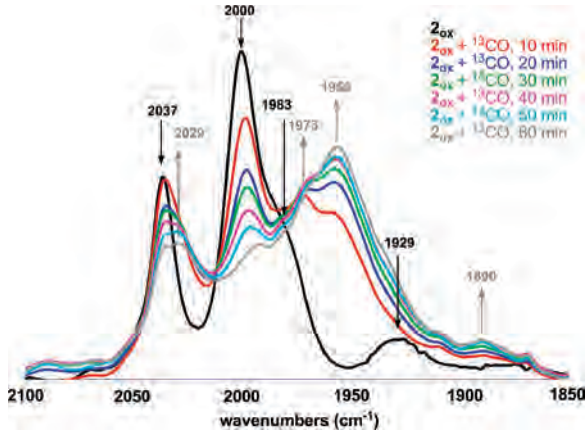

Figure 9. IR spectra monitoring the reaction of $\mathbf{2_{ox}}$ with ^{13}CO at −78 °C in CH_2Cl_2 over a 1 h time period in the absence of light.

Scheme 5

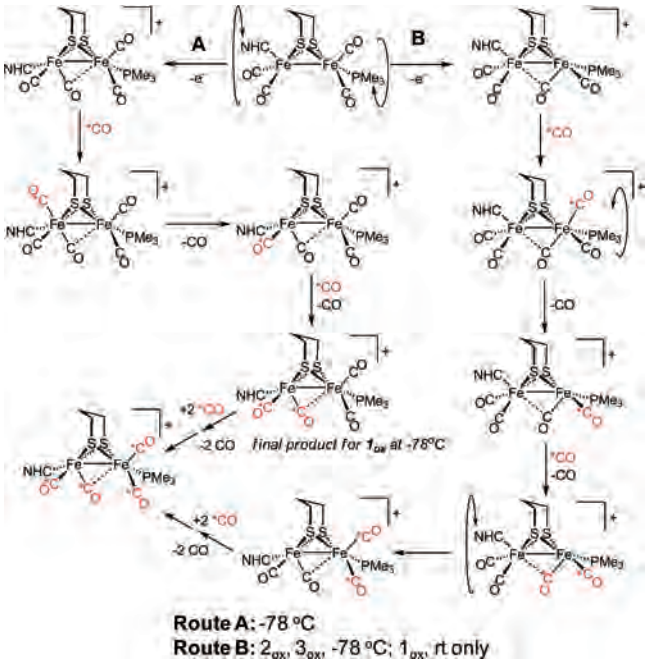

(m), 1957 (vs), 1940 (sh), and 1888 (w) cm^{-1}. Thus, the new major ν(CO) stretches at 1958 and 1890 cm^{-1} can be attributed to fully labeled $\mathbf{2_{ox}}$, the expected band at 1993 cm^{-1} is likely present underneath the 2000 cm^{-1} band of the starting material. The formation of fully ^{13}CO-labeled $\mathbf{2_{ox}}$ likely proceeds via the same mechanism proposed for $\mathbf{1_{ox}}$,; however the barrier to rotation at both Fe centers is sufficiently low to provide two different pathways following the loss of the bridging CO (Scheme 6). Another possible variation of this mechanism by which ^{13}CO could exchange to both sites is shown as path **B** in Scheme 5. In this path, extrinsic ^{13}CO binding induces the semibridging CO ligand to migrate to the second Fe center with concomitant loss of ^{12}CO.

The following experiments were performed to shed some light on the assignment of the IR stretches at 2029 and 1973 cm^{-1}, which cannot be assigned as either starting material ($\mathbf{2_{ox}}$) or product (^{13}CO-labeled $\mathbf{2_{ox}}$) in the ^{13}CO exchange reaction with $\mathbf{2_{ox}}$. After 60 min of exposure to ^{13}CO, the resulting solution of labeled $\mathbf{2_{ox}}$ was reduced with $CoCp_2$ at −78 °C (eq 1). New bands attributed to the neutral Fe^IFe^I complex **2** appeared at 1932, 1896 cm^{-1} (calcd: 1931, 1892, 1857, 1843 cm^{-1}), but the bands at 2029 and 1973 cm^{-1} persisted (Figure 10). Exposure of $\mathbf{2_{ox}}$ to ^{13}CO for 60 min at −78 °C followed by bubbling of ^{12}CO through the resulting solution for 30 min resulted in a single species identified by IR spectroscopy: the bands at 2021 and 1996 cm^{-1} are attributed to exclusive formation of $\mathbf{2_{ox}^{CO}}$ (Figure 10, eq 2). Because the unidentified species with bands at 2029 and 1973 cm^{-1} is not reduced by $CoCp_2$ ($E° = -1.33$ V vs Fc/Fc^+) and reacts with ^{12}CO to generate the CO-adduct $\mathbf{2_{ox}^{CO}}$, we assign this species as a ^{13}CO-adduct, $\mathbf{2_{ox}}^{13}CO$.

$$\text{mixture } ^{13}\text{CO-labeled products} + CoCp_2 \rightarrow \mathbf{2} + \mathbf{2_{ox}}^{13CO} \quad (1)$$

$$\text{mixture } ^{13}\text{CO-labeled products} + ^{12}CO \rightarrow \mathbf{2_{ox}}^{CO} \quad (2)$$

In conclusion, the inherent differences between $\mathbf{1_{ox}}$ and its less sterically hindered congeners $\mathbf{2_{ox}}$ and $\mathbf{3_{ox}}$ lead to distinctly different reactivity of these complexes toward extrinsic CO. While $\mathbf{2_{ox}}$ and $\mathbf{3_{ox}}$ readily bind an additional CO ligand, complex $\mathbf{1_{ox}}$ reacts sluggishly with excess CO. In addition, while regioselective exchange with ^{13}CO is observed at −78 °C for $\mathbf{1_{ox}}$, ^{13}CO scrambles into all positions of $\mathbf{2_{ox}}$ even at low temperatures, with formation of an intermediate ^{13}CO adduct observed by IR spectroscopy. This confirms our proposed associative mechanism for ^{13}CO exchange—the nonregioselective ^{13}CO scrambling into $\mathbf{2_{ox}}$ is likely a result of more fluxionality in this less sterically hindered derivative (i.e., the barrier to rotation at both Fe centers is low, vide infra).

Computational Investigations Using DFT. To complement our experimental investigations of the rotated mixed valent $Fe^{II}Fe^I$ models, these complexes have been examined using DFT. Results from a preliminary computational study of the IMes derivative indicated that the unpaired spin density in the $S = {}^1/_2$ complex lies mostly on the rotated iron center, indicating that the oxidation state assignment is (IMes)(CO)$Fe^I(\mu$-CO)(μ-pdt)Fe^{II}(PMe_3)$(CO)_2$.[15] In addition, examination of the frontier molecular orbitals of the neutral and cationic complexes indicated that rotation about the $(IMes)(CO)_2Fe$ center leads to a disruption in the Fe^I-Fe^I bond, raising the energy of the highest occupied molecular orbital (HOMO) and stabilizing the oxidized, mixed valent species (Figure 11). We turn our attention now to a more detailed investigation of these $Fe^{II}Fe^I$ complexes, with the ultimate goal of providing an explanation for the spectroscopic, and, perhaps, structural differences between the three NHC derivatives as well as their different reactivities toward extrinsic CO.

As noted in the Experimental Section of this manuscript, the mixed valent IMes derivative $\mathbf{1_{ox}}$, whose structure is known definitively (X-ray), possesses distinctly different spectroscopic features (IR, EPR) from the IMesMe and IMe derivatives $\mathbf{2_{ox}}$ and $\mathbf{3_{ox}}$. In particular, the IR spectrum of $\mathbf{1_{ox}}$ features a ν(CO) stretch corresponding to the semibridging CO at 1861 cm^{-1} while the lowest energy bands in the IR spectra of $\mathbf{2_{ox}}$ and $\mathbf{3_{ox}}$ are at 1929 and 1930 cm^{-1}, respectively. These spectroscopic differences suggest that $\mathbf{2_{ox}}$ and

Scheme 6

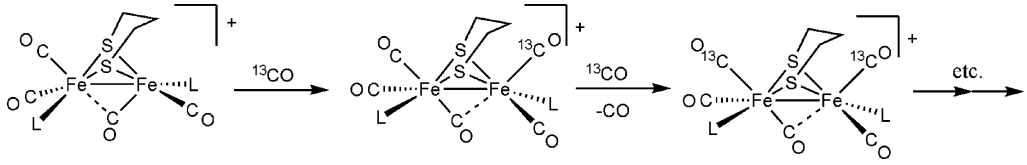

$\mathbf{3_{ox}}$ adopt a different structure from their structurally characterized analogue $\mathbf{1_{ox}}$. In light of our inability to obtain single crystals of either $\mathbf{2_{ox}}$ or $\mathbf{3_{ox}}$, we have turned to DFT to get a better idea of the most likely structure adopted by these two mixed valent derivatives.

Starting from rotated structures similar to that determined crystallographically for $\mathbf{1_{ox}}$, and fully corroborated by DFT calculations,[15] geometry optimizations and vibrational frequency calculations were carried out on $\mathbf{1_{ox}}$, $\mathbf{2_{ox}}$, and $\mathbf{3_{ox}}$ using the B3LYP functional with modified LANL2DZ basis sets on the Fe, S, and P atoms and the D95 basis set on all C, N, O, and H atoms.[15] In all three derivatives, a rotated structure with a semibridging carbonyl, nearly identical to the experimental structure of $\mathbf{1_{ox}}$, was found as a minimum, with the unpaired spin density lying almost entirely on the rotated iron center. In fact, geometry optimization of $\mathbf{3_{ox}}$ starting from an unrotated geometry, as in the $Fe^{I}Fe^{I}$ complex **3**, leads to the same structure obtained if starting from a rotated geometry. The geometric parameters calculated for $\mathbf{1_{ox}}$, $\mathbf{2_{ox}}$, and $\mathbf{3_{ox}}$ are similar (Table 4), with the most variations occurring in the parameters associated with the semibridging carbonyl moiety. An interesting variation in these structures is the orientation of the NHC (i.e., the CN_2C_2 plane formed by the 5-membered imidazolylidene ring). By both calculation and experiment, the carbene in $\mathbf{1_{ox}}$ is oriented such that the CN_2C_2 plane eclipses the Fe−S bond vector trans to it. In $\mathbf{3_{ox}}$, however, the carbene plane is calculated to be tilted 27° away from the Fe−S vector. In the case of the asymmetric IMesMe derivative $\mathbf{2_{ox}}$, rotation of the carbene about the Fe−C bond leads to two potential isomers: one in which the NHC mesityl group points upward in the direction of the dithiolate linker and another in which the mesityl group points down toward the semibridging CO. Both potential isomers were calculated, and it was found that the "up" isomer is more stable while the "down" isomer is a transition state at slightly higher energy ($\Delta G° = 1.5$ kcal/mol). In general, the barrier to rotation about the $Fe-C_{NHC}$ bond is low, as has been observed for other transition metal NHC complexes.[14] The vibrational frequencies calculated for the terminal CO ligands of $\mathbf{1_{ox}}$ agree reasonably well with experiment when a minimal scaling factor is used (Table 5).[49] However, the stretching frequency predicted for the bridging CO ligand (1836 cm^{-1}) is substantially lower than the experimental value (1861 cm^{-1}). Similar difficulties in predicting the ν(CO) stretches of bridging carbonyl ligands using DFT calculations have been previously documented.[50] The calculated vibrational frequencies for the terminal CO ligands of $\mathbf{2_{ox}}$ and $\mathbf{3_{ox}}$ also agree remarkably well with experiment; however, the calculations find low frequency bands at 1803 and 1836 cm^{-1} for $\mathbf{2_{ox}}$ and $\mathbf{3_{ox}}$, respectively,

Table 4. Unpaired Spin Density and Relevant Geometrical Parameters Calculated for $\mathbf{1_{ox}}$−$\mathbf{3_{ox}}$ Starting from the Crystallographic Coordinates of $\mathbf{1_{ox}}$

	spin density (Fe2/Fe1)[a]	Fe1−CO_{br}	Fe2−CO_{br}	Fe2−C−O	Fe1−Fe2
$\mathbf{1_{ox}}$	1.18/0.00	2.162 Å	1.881 Å	149.1°	2.611 Å
$\mathbf{2_{ox}}$	1.28/−0.04	2.162 Å	1.904 Å	144.5°	2.624 Å
$\mathbf{3_{ox}}$	1.17/0.00	2.224 Å	1.852 Å	150.8°	2.584 Å

[a] Fe1 refers to the PMe_3-ligated Fe atom, while Fe2 refers to the NHC-bound Fe center.

Table 5. Calculated [a] and Experimental ν(CO) Stretching Frequencies for Complexes $\mathbf{1_{ox}}$−$\mathbf{3_{ox}}$

	calculated (cm^{-1})	experimental (cm^{-1})
$\mathbf{1_{ox}}$	2030, 1993, 1993, 1836	2037, 1997, 1987, 1861
$\mathbf{2_{ox}}$	2035, 1997, 1993, 1803	2036, 2000, 1983, 1929
$\mathbf{3_{ox}}$	2035, 2004, 1999, 1836	2036, 2005, 1981, 1929

[a] Using a scaling factor of 1.0107.

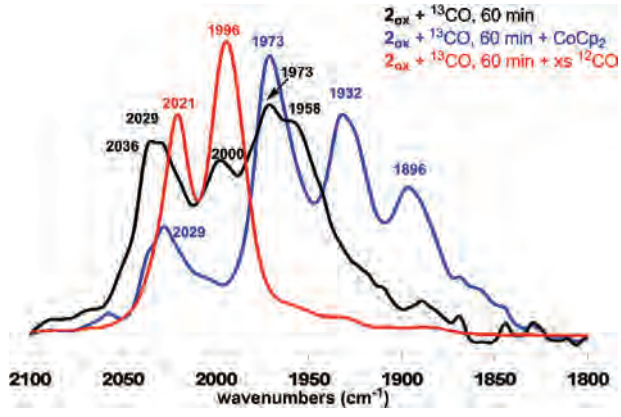

Figure 10. IR spectra of the mixture of isotopically labeled product formed upon exposure of $\mathbf{2_{ox}}$ to ^{13}CO (black), and the products of reaction of this mixture with $CoCp_2$ (blue) and excess ^{12}CO (red).

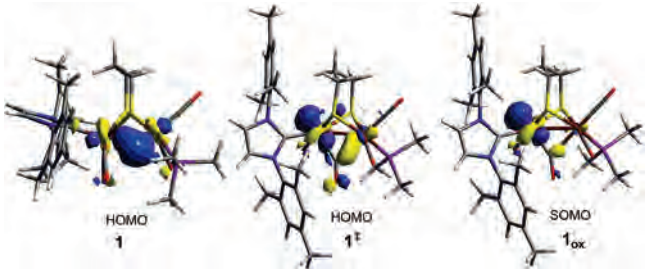

Figure 11. Pictorial representations of the HOMOs (or SOMO, in the case of $\mathbf{1_{ox}}$) of the neutral complex **1**, the rotated transition state $\mathbf{1^{‡}}$, and the cation $\mathbf{1_{ox}}$.

(47) Roseboom, W.; De Lacey, A. L.; Fernandez, V. M.; Hatchikian, E. C.; Albracht, S. P. J. *J. Biol. Inorg. Chem.* **2006**, *11*, 102–108.
(48) Justice, A. K.; Nilges, M. J.; Rauchfuss, T. B.; Wilson, S. R.; De Gioia, L.; Zampella, G. *J. Am. Chem. Soc.* [Online early access]. DOI: 10.102/ja7113008.
(49) A scaling factor of 1.0107 was determined by plotting the experimental vibrational frequencies for **1** vs those calculated using an identical computational method ($\nu(CO)_{exp} = 1.0107\nu(CO)_{calc}$, $R = 0.99$).
(50) Tye, J. W.; Darensbourg, M. Y.; Hall, M. B. *J. Comput. Chem.* **2006**, *27*, 1254–1462.

Scheme 7. Eight Possible Conformational Isomers of $\mathbf{3_{ox}}$ and Their Relative Energies (G°) and Unpaired Spin Densities (in Italics)

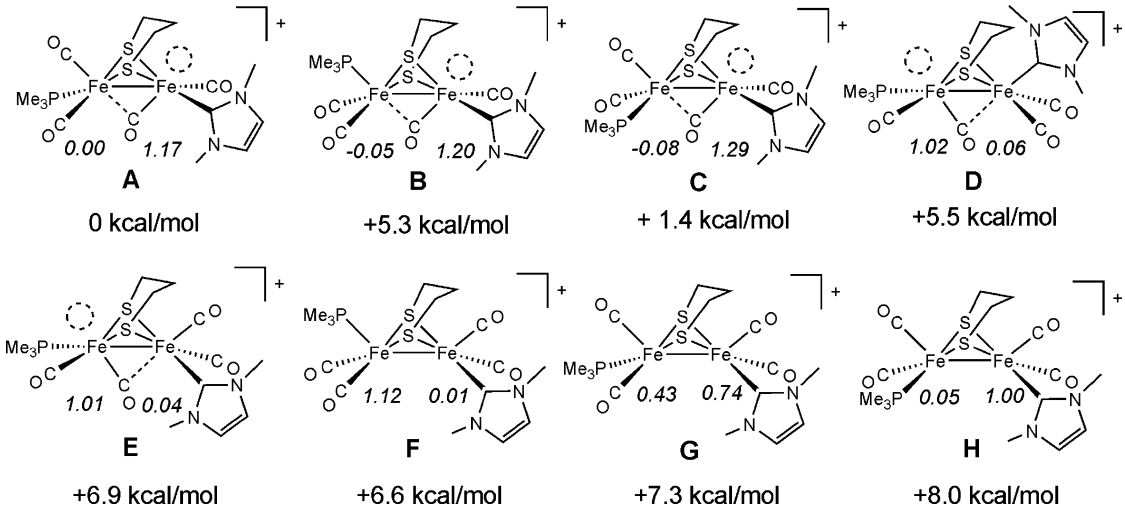

values which are some 100 cm^{-1} lower than the lowest ν(CO) measured in solution (1929 cm^{-1} for both $\mathbf{2_{ox}}$ and $\mathbf{3_{ox}}$). This discrepancy between theory and experiment led us to examine a number of other potential structural isomers of $\mathbf{3_{ox}}$ to ascertain whether other low energy structures might be accessed that would yield more compatible ν(CO) values. Considering both rotated and unrotated structures, there are 11 possible conformational isomers of $\mathbf{3_{ox}}$, differing in the relative apical or basal positions of the NHC and PMe_3 ligands (see Supporting Information). Upon full geometry optimization using DFT (B3LYP), two of the unrotated/eclipsed isomers, including the aforementioned structure identical to the neutral precursor **3**, spontaneously adopted rotated structures. In addition, optimization of one of the possible rotated structures led to an unrotated geometry as a minimum. Thus, only the eight structural isomers of $\mathbf{3_{ox}}$ shown in Scheme 7 will be considered as minima. The ring flip of the metallothiacyclohexane ring was found to be worth a mere ~1−2 kcal/mol (see Supporting Information), so for simplicity our discussion here will be limited to isomers in which the central methylene group points toward the NHC-coordinated Fe center. Five of the possible structures of $\mathbf{3_{ox}}$ feature a rotated geometry at one of the Fe centers (Scheme 7, **A**−**E**). The isomer calculated to be most stable is **A**, in which the NHC-bound Fe center rotates and the PMe_3 ligand maintains a basal position *trans*-oid to the NHC. The corresponding *cis*-oid isomer, **C**, is 1.4 kcal/mol higher in energy, while the isomer with PMe_3 in an apical position is 5.3 kcal/mol higher in energy. Two possible isomers in which the ligands about the PMe_3-substituted Fe center rotate, one with the NHC in an apical position (**D**) and one with a basal NHC (**E**), were calculated to be higher in energy than **A** by 5.5 and 6.9 kcal/mol, respectively. Notably, in some of these rotated possibilities, the unpaired spin density resides almost exclusively on the rotated Fe center (Scheme 7, italics). The optimized structures of **A**−**E** differ substantially, particularly with respect to the bridging CO ligand (Table 6). *Indeed, the Fe−C−O angle varies over a range of 20°, and the distance between the unrotated Fe center and the C atom of the μ-CO varies over a range of 0.7 Å in the structural isomers of* $\mathbf{3^{ox}}$ *calculated.*

Table 6. Relevant Geometrical Parameters Calculated for the Eight Possible Conformational Isomers of $\mathbf{3_{ox}}$ in Both Rotated and Unrotated Structures

	Fe1−CO	Fe2−CO	Fe2−C−O	Fe1−Fe2
A	2.224 Å	1.852 Å	150.8°	2.584 Å
B	2.550 Å	1.820 Å	164.7°	2.583 Å
C	2.182 Å	1.863 Å	147.9°	2.578 Å
D	1.817 Å	2.590 Å	164.9°	2.634 Å
E	1.798 Å	2.919 Å	170.6°	2.707 Å
F	1.813 Å	2.949 Å	169.7°	2.685 Å
G	1.791 Å	3.533 Å	179.1°	2.666 Å
H	1.798 Å	3.106 Å	173.9°	2.747 Å

The other three possibilities possess an unrotated geometry (Scheme 7, **F**−**H**) and are all higher in energy than the lowest energy rotated isomer (**A**). It is noteworthy that in all three unrotated isomers the NHC occupies a basal position: initial geometries with the NHC in an apical position lead to rotation during geometry optimization. The optimized structures of **F**−**H** reveal a slight rotation, such that the ligands about the two Fe centers no longer eclipse each other; however, there is no evidence for a semibridging carbonyl ligand or an open coordination site in these structures. The unrotated isomer in which the PMe_3 ligand is apical while the NHC ligand is basal (**F**) is 6.6 kcal/mol higher in energy than **A** while the *trans*-oid (**G**) and *cis*-oid (**H**) basal/basal isomers are even higher in energy (7.3 and 8.0 kcal/mol, respectively). The location of the unpaired spin density is less predictable in these isomers: in **F** the unpaired spin resides on the PMe_3-substituted Fe, in **H** the unpaired spin resides on the NHC-substituted Fe, and in **G** the unpaired electron is distributed over both Fe centers. The optimized geometries of **F**−**H** feature nearly linear Fe−C−O angles and relatively long Fe−Fe bond lengths (Table 6).

The significant structural differences in the optimized geometries of isomers **A**−**H** lead to dramatic differences in their calculated ν(CO) stretching frequencies (Table 7). While the three highest energy computed ν(CO) stretches vary by only 10−15 cm^{-1} and agree well with experiment, substantial differences are seen in the calculated positions of the lowest frequency band (Table 7). As mentioned previously, the

Table 7. Calculated ν(CO) Stretching Frequencies for Isomers **A**−**H**[a]

	ν(CO) (cm^{-1})			
A	2035	2004	1999	*1836*
B	2038	2008	2000	*1913*
C	2039	2011	2000	*1823*
D	2044	2006	2000	*1910*
E	2028	1991	1989	*1925*
F	2034	1994	1990	*1929*
G	2037	1993	1988	*1931*
H	2018	1993	1979	*1964*

[a] Using a scaling factor of 1.0107.

lowest frequency band calculated for the isomer **A** (1836 cm^{-1}) agrees poorly with the experimentally observed CO vibration for $\mathbf{3_{ox}}$ (1929 cm^{-1}). The calculated low frequency ν(CO) band for the isomer closest in energy (**C**, 1823 cm^{-1}) is also significantly lower than the observed frequency. On the other hand, the lowest frequency CO stretch calculated for unrotated isomer **H** (1964 cm^{-1}) is much higher than that observed experimentally. The remaining structural isomers have a computed low frequency at 1913 cm^{-1} (**B**), 1910 cm^{-1} (**D**), 1925 cm^{-1} (**E**), 1929 cm^{-1} (**F**), and 1931 cm^{-1} (**G**) and thus show better agreement with experiment (ν(CO) = 1929 cm^{-1}). However, because all of these isomers are higher in energy than **A**, there is insufficient evidence to assign $\mathbf{3_{ox}}$ as one of these alternative structural isomers. It should be noted that the use of different density functionals and different basis sets leads to similar energy differences between the possible isomers of $\mathbf{3_{ox}}$ (see Supporting Information). On the other hand, the vibrational frequencies are much more sensitive to different functionals, basis sets, and small structural changes; for example, with respect to relative frequency of the semibridging CO, flipping the metallothiacyclohexane ring causes a shift of ∼40 cm^{-1} to higher frequency, and the larger basis sets causes a shift of ∼20 cm^{-1} to higher frequency (see Supporting Information). In general, it appears that both the structural parameters and the vibrational frequencies associated with the semibridging CO ligand are remarkably sensitive to details of the electronic and molecular structure.

It is also interesting to note that, while rotation of the carbene side of these mixed valent cations is always preferred, the extent to which this isomer is favored varies with the identity of the NHC ligand. As mentioned in the preceding paragraphs, the rotated NHC-substituted Fe side is favored by 5.5 kcal/mol in the IMe derivative $\mathbf{3_{ox}}$. However, this energy difference increases to 6.5 kcal/mol with the IMesMe derivative $\mathbf{2_{ox}}$ and to 10.1 kcal/mol for the IMes derivative $\mathbf{1_{ox}}$. Thus, the NHC-substituted Fe center rotation is favored in the order $\mathbf{1_{ox}} \gg \mathbf{2_{ox}} > \mathbf{3_{ox}}$. On the basis of this trend, as well as the preference for the more sterically bulky N-substituent in $\mathbf{2_{ox}}$ to point upward toward the open coordination site, a reasonable conclusion is that steric protection of the open coordination site plays an important role in stabilizing the rotated geometry of these mixed valent derivatives.

Computations were also used to examine the binding of extrinsic CO to $\mathbf{3_{ox}}$. As noted in the Experimental Section, $\mathbf{3_{ox}}$ reversibly binds extrinsic CO to generate a new $S = {}^1/_2$ species, $\mathbf{3_{ox}}^{\mathbf{CO}}$ with a distinctly different IR spectrum than

Scheme 8

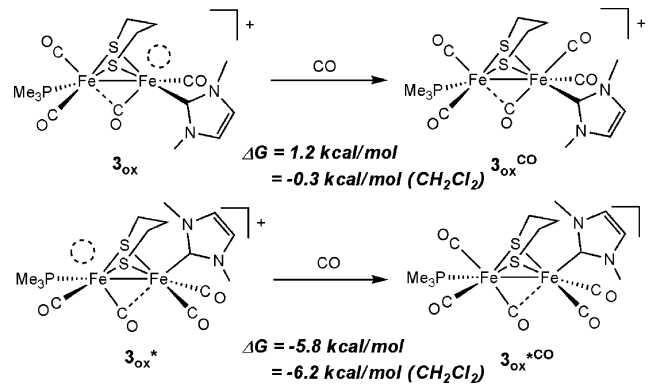

Table 8. Relevant Bond Distances and Angles Calculated for the Two Possible CO Adducts, $\mathbf{3_{ox}}^{\mathbf{CO}}$ and $\mathbf{3_{ox}}^{\mathbf{*CO}}$

	Fe1−C$_{br}$	Fe2−C$_{br}$	Fe2−C−O	Fe1−C−O	Fe1−Fe2
$\mathbf{3_{ox}}^{\mathbf{CO}}$	2.020 Å	2.020 Å	136.3°	136.3°	2.793 Å
$\mathbf{3_{ox}}^{\mathbf{*CO}}$	1.983 Å	2.074 Å	133.3°	138.7°	2.820 Å

that of $\mathbf{3_{ox}}$. Because isomers of $\mathbf{3_{ox}}$ in which the IMe and PMe_3 side rotate are relatively close in energy (∼5 kcal/mol), two possible isomers of the CO adduct can be envisioned: one in which CO is bound to the IMe-substituted Fe center, $\mathbf{3_{ox}}^{\mathbf{CO}}$, and one in which CO is bound to the PMe_3-substituted Fe center, $\mathbf{3_{ox}}^{\mathbf{*CO}}$. As shown in Scheme 8, CO binding to an isomer in which the PMe_3 side is rotated, $\mathbf{3_{ox}}$*, is energetically favorable, while CO binding to $\mathbf{3_{ox}}$ is essentially energetically neutral. Thus, calculations suggest that the CO adducts observed experimentally upon binding of CO to $\mathbf{2_{ox}}$ and $\mathbf{3_{ox}}$ have CO bound to the PMe_3-substituted Fe center. This hypothesis is consistent with several experimental observations, including: (1) the ^{31}P superhyperfine coupling observed in the EPR spectrum of the CO adduct $\mathbf{2_{ox}}^{\mathbf{CO}}$ that is not observed in the EPR spectrum of the precursor $\mathbf{2_{ox}}$, and (2) the propensity of $\mathbf{2_{ox}}$ and $\mathbf{3_{ox}}$ to bind CO much more readily than $\mathbf{1_{ox}}$: rotation of the PMe_3 side of the molecule must occur before CO binding becomes favorable, and this rotation is ∼5 kcal/mol more uphill for $\mathbf{1_{ox}}$.

The structural parameters and electron distribution in the optimized structures of the CO adducts $\mathbf{3_{ox}}^{\mathbf{CO}}$ and $\mathbf{3_{ox}}^{\mathbf{*CO}}$ are also worthy of discussion. Relevant bond distances and angles are tabulated in Table 8. Interestingly, upon binding of extrinsic CO, the semibridging CO becomes fully bridging. In the isomer in which CO binds to the IMe-substituted Fe ($\mathbf{3_{ox}}^{\mathbf{CO}}$), the geometry about the μ-CO is completely symmetric, with identical Fe−C distances (2.020 Å) and Fe−C−O angles (136.3°). On the other hand, the μ-CO geometry is slightly asymmetric in $\mathbf{3_{ox}}^{\mathbf{*CO}}$, with the bridging CO remaining slightly more tightly bound to the PMe_3-substituted side.

These changes in geometry are accompanied by more symmetrical electron delocalization for both isomers $\mathbf{3_{ox}}^{\mathbf{CO}}$ and $\mathbf{3_{ox}}^{\mathbf{*CO}}$. The unpaired spin density in both structural isomers is distributed over both Fe centers with a substantial spin population on the carbon and oxygen atoms of the bridging carbonyl (see Supporting Information, Figure S3). Consistent with the more symmetric structure predicted for

Scheme 9

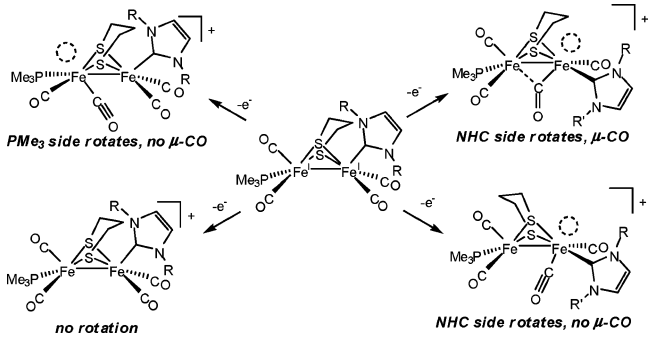

$\mathbf{3_{ox}}^{CO}$, the unpaired spin is localized equally on both Fe centers, while the unpaired electron of $\mathbf{3_{ox}}^{*CO}$ is delocalized in a more asymmetric fashion, with slightly more spin density on the IMe-substituted Fe center. The Fe oxidation states in each of these CO adducts are better described as $Fe^{1.5}Fe^{1.5}$, in contrast to the $Fe^{II}Fe^{I}$ oxidation state assignment for the precursor $\mathbf{3_{ox}}$. This electronic delocalization is also reflected in the frontier molecular orbitals of the CO adducts, illustrated for $\mathbf{3_{ox}}^{CO}$ (see Supporting Information, Figure S3). Both the HOMO (SOMO) and lowest unoccupied molecular orbital (LUMO) are delocalized symmetrically over both of the iron centers, as well as the bridging CO moiety.

The computational results regarding electronic delocalization in the CO adduct can be used to rationalize the shifts in IR CO stretching frequencies experimentally observed upon CO binding. The symmetric and asymmetric stretches associated with the terminal CO ligands on the $(CO)_2(PMe_3)Fe$ unit in $\mathbf{3_{ox}}$ (2036 cm^{-1} and 1983 cm^{-1}, respectively) would be expected to shift to lower frequencies upon a change in oxidation state from Fe^{II} to $Fe^{1.5}$ once CO is bound. Simultaneously, the band associated with the terminal CO ligand on the $(CO)_2(IMe)Fe$ unit (2004 cm^{-1}) should split into a symmetric and asymmetric stretch and shift to higher frequency with binding of extrinsic CO.

Conclusions and Comments

From the above serial approach to establishing fundamental properties of the diiron-dithiolate complexes which have certain features in common with the $[FeFe]H_2$ase active site the following salient points are noted:

• The N-heterocyclic carbene ligands IMes, IMesMe, and IMe ligands are effectual in accessing thermally and moderately air-stable heteroligated $(\mu\text{-pdt})[Fe^{I}(CO)_2PMe_3][Fe^{I}(CO)_2NHC]$ complexes in which the PMe_3 and NHC ligands are of sufficient donating abilities to stabilize a one-electron oxidized form (Scheme 9). At the reduced $Fe^{I}Fe^{I}$ redox level, the complexes crystallize as identical conformational isomers. At the $Fe^{I}Fe^{II}$ level, only the complex $\mathbf{1_{ox}}$ has yielded to crystallization, and it adopts a rotated structure with semibridging carbonyl remarkably analogous to the two-iron subsite of H_{ox}.

• Consistent with literature reports of the properties of NHC ligands in monometallic complexes,[51] changes in R-group substitution at N in the NHC ligands have minimal effect on the donor abilities of such ligands as evidenced by ν(CO) IR spectroscopy of members of the series. The complexes differ from one another only in the steric bulk which flanks the carbene carbon donor site.

• Assuming (from the ν(CO) IR data of the $Fe^{I}Fe^{I}$ complexes) differences in electron density at iron are small within the series, we are led to the conclusion that disparities in the accessibility and reversibility of the $Fe^{I}Fe^{I}/Fe^{II}Fe^{I}$ redox couple, decreasing in the order **1** > **2** > **3**, must be due to steric differences in the substituent NHC ligands. These differences might determine (a) stabilization of the rotated $Fe^{I}Fe^{II}$ product imparted from steric protection of the "open" site by, in the case of $\mathbf{1_{ox}}$, an aryl group; or, (b) stability of conformational isomers for various rotated or unrotated structural possibilities for the product (Scheme 8).

• There is an impressive variation in solution structures and stabilities of the $Fe^{I}Fe^{II}$ complexes that also relates to steric differences of the NHC ligands. The IMe and IMesMe derivatives do not display the low energy ν(CO) band (at ca. 1860 cm^{-1}) that characterizes the semibridging CO group in the IMes derivative, $\mathbf{1_{ox}}$. Likewise, differences in the EPR spectra of $\mathbf{2_{ox}}$ and $\mathbf{3_{ox}}$ indicate that the unpaired electron is in a different environment and may not be localized on a single Fe atom as in $\mathbf{1_{ox}}$.

• DFT calculations predict the lowest energy structure of all NHC derivatives to be of the rotated type with a semibridging carbonyl arising from the rotated $Fe(CO)_2$(NHC) unit, $(\mu\text{-pdt})(\mu\text{-CO})[Fe^{II}(CO)_2PMe_3][Fe^{I}(CO)(NHC)]^+$, that is, the same as the experimentally found structure that exists both in solid and in solution for the IMes derivative $\mathbf{1_{ox}}$ and with the same assignment of oxidation state from the calculated unpaired electron density. Nevertheless, for the less sterically hindered $\mathbf{2_{ox}}$ and $\mathbf{3_{ox}}$ derivatives this rotated structure is inconsistent with experimental (solution IR) data. A number of structural isomers calculated to check both rotated and unrotated geometries at either iron center are within 7 kcal/mol in energy and match the IR data more closely.

• Reversible formation of a CO adduct is seen in all three $Fe^{I}Fe^{II}$ derivatives, with order of stability as follows: $\mathbf{3_{ox}} \geq \mathbf{2_{ox}} \gg \mathbf{1_{ox}}$. We suggest this CO adduct is pivotal in the ^{13}CO exchange process which is regioselective for $\mathbf{1_{ox}}$ at −78 °C but not for $\mathbf{3_{ox}}$ or $\mathbf{2_{ox}}$ under the same conditions. Thus, we conclude that the open site in $\mathbf{1_{ox}}$ is sterically protected by its larger NHC ligand.

The rotated structure of a mixed-valent $Fe^{I}Fe^{II}$ from the Rauchfuss group, $(\mu\text{-}S_2C_2H_4)[Fe(CO)_2PMe_3][Fe(CO)(dppv)]^+$, bears similarity to $\mathbf{1_{ox}}$ in that the dppv ligand also has aryl rings which are directed toward the open site of the rotated iron, presumably offering steric protection/stabilization.[10] It differs from $\mathbf{1_{ox}}$ in that the CO that lies under the Fe−Fe vector is nearly linear, and consistently, the lowest energy ν(CO) IR band at 1883 cm^{-1} is higher than that from the semibridging CO ligand of $\mathbf{1_{ox}}$. It is clear that the synthetic, abiological ligands chosen by Rauchfuss and by us yield analogues in coordination and basic Fe_2S_2 framework to that adopted by nature for the $[FeFe]H_2$ase active site. The

(51) Fürstner, A.; Alcarazo, M.; Krause, H.; Lehmann, C. W. *J. Am. Chem. Soc.* **2007**, *129*, 12676–12677.

composition is remarkably sensitive to ligands that provide intramolecular interactions, displayed in the synthetic analogues by aryl groups. As shown in Scheme 1, in the mixed valent, rotated form of diiron units an Fe^{I} is primed to be reduced and protonated, an electron/proton coupled process, producing a terminal $Fe^{II}-H$. Alternatively with little structural reorganization, the same penta-coordinate Fe^{I} can have an electron withdrawn and become a coordinatively unsaturated Fe^{II} with ideal Lewis acidity to bind H_2 and begin the H_2 cleavage reaction required for the known reversible activity of the enzyme.

Note that the enzyme possesses a 4Fe4S redox active unit directly attached to the Fe subsite whose influence on the distal iron can change the potential for e^-/H^+ attraction. As found by Brunold and co-workers, this iron sulfur cluster also plays an important role in modulating the geometric and electronic structure of the 2Fe2S subsite of the H cluster.[52] The current models, successful as they are in mimicking structural features, do not have this capacity. Nevertheless, the sterically encumbered NHC ligand IMes appears to fulfill some of the second coordination sphere requirements that exist in the enzyme in the form of ^{234}Pro and ^{417}Phe residues close to the open site of the distal iron.[2] Evidently, the protein matrix is sufficient to maintain this rotated structure throughout various redox levels through either hydrogen bonding or steric interactions; however, the mixed valent model complexes known to date return to their unrotated form upon re-reduction. The current study thus highlights two future challenges for developing more accurate molecular models of the active site of [FeFe]-H_2ase: (1) replacement of PMe_3 by a redox active ligand, and (2) the development of an intra- or intermolecular means for locking the rotated structure into place.

In conclusion, a comment regarding the difference between the three members of the NHC series is appropriate. Electron spin resonance and ν(CO) IR spectral data recorded in solution may be readily interpreted according to the solid state structure of $\mathbf{1_{ox}}$. DFT calculations are consistent with a mixed valent Fe(II)Fe(I) compound with charge separation and the unpaired electron localized on the rotated iron. In addition, DFT calculations provide a reasonable match of the ν(CO) IR spectrum. While the derivative with only one mesityl group and one Me substituent on the imidazolium nitrogens, $\mathbf{2_{ox}}$, would have the capability to provide the same steric protection of the open site by orienting the mesityl group over the rotated iron, such a structure was not observed. Nevertheless, the DFT calculation suggested a structure similar to $\mathbf{1_{ox}}$ as the lowest energy form for both $\mathbf{2_{ox}}$ and $\mathbf{3_{ox}}$. However, other theoretical structures are now closer in energy for the less bulky NHC derivatives. Furthermore, from experiments, the IR band corresponding to the semibridging CO was not observed for $\mathbf{2_{ox}}$ or $\mathbf{3_{ox}}$, and the EPR spectrum showed a significantly broader signal. Hence, the less sterically hindered NHC ligands, rather than locking in a single stable structure, may provide a plethora of other possibilities, summarized in Scheme 9.

Acknowledgment. The authors gratefully acknowledge financial support of this work from the National Science Foundation (CHE-0616695 to M.Y.D. and CHE-0518047 to M.B.H.) with contributions from the R. A. Welch Foundation (A-0924 to M.Y.D. and A-0648 to M.B.H.). We also thank Ren Miao, Jessica Garber, and Paul Lindahl for assistance with EPR spectroscopy.

Note Added after ASAP Publication. This article was published ASAP on July 3, 2008, with one of the author names misspelled and a minor text correction. The correct version was published on July 28, 2008.

Supporting Information Available: Crystallographic data for $\mathbf{2_{NHC}}$, **2**, and **3** (in both table and CIF format), additional electrochemical data, electrospray mass spectrum of $\mathbf{1_{ox}}$, and additional information and data related to the DFT calculations (PDF). This material is available free of charge via the Internet at http://pubs.acs.org.

IC800654A

(52) Fiedler, A. T.; Brunold, T. C. *Inorg. Chem.* **2005**, *44*, 9322–9344.